SPRINGER BRIEFS IN APPLIED SCIENCES AND TECHNOLOGY
SPRINGER BRIEFS IN THERMAL ENGINEERING AND APPLIED SCIENCE

Sean C. Garrick
Michael Bühlmann

Modeling of Gas-to-Particle Mass Transfer in Turbulent Flows

Springer

SpringerBriefs in Applied Sciences and Technology

SpringerBriefs in Thermal Engineering and Applied Science

Series editor
Janusz Kacprzyk, Polish Academy of Sciences, Systems Research Institute,
Warsaw, Poland

SpringerBriefs present concise summaries of cutting-edge research and practical applications across a wide spectrum of fields. Featuring compact volumes of 50 to 125 pages, the series covers a range of content from professional to academic.
Typical publications can be:

- A timely report of state-of-the art methods
- An introduction to or a manual for the application of mathematical or computer techniques
- A bridge between new research results, as published in journal articles
- A snapshot of a hot or emerging topic
- An in-depth case study
- A presentation of core concepts that students must understand in order to make independent contributions

SpringerBriefs are characterized by fast, global electronic dissemination, standard publishing contracts, standardized manuscript preparation and formatting guidelines, and expedited production schedules.

On the one hand, **SpringerBriefs in Applied Sciences and Technology** are devoted to the publication of fundamentals and applications within the different classical engineering disciplines as well as in interdisciplinary fields that recently emerged between these areas. On the other hand, as the boundary separating fundamental research and applied technology is more and more dissolving, this series is particularly open to trans-disciplinary topics between fundamental science and engineering.

Indexed by EI-Compendex and Springerlink

More information about this series at http://www.springer.com/series/8884

Sean C. Garrick • Michael Bühlmann

Modeling of Gas-to-Particle Mass Transfer in Turbulent Flows

Springer

Sean C. Garrick
Department of Mechanical Engineering
University of Minnesota
Minneapolis, MN, USA

Michael Bühlmann
University of Minnesota
Minneapolis, MN, USA

ISSN 2191-530X ISSN 2191-5318 (electronic)
SpringerBriefs in Applied Sciences and Technology
ISSN 2193-2530 ISSN 2193-2549 (electronic)
SpringerBriefs in Thermal Engineering and Applied Science
ISBN 978-3-319-59583-2 ISBN 978-3-319-59584-9 (eBook)
DOI 10.1007/978-3-319-59584-9

Library of Congress Control Number: 2017943675

© The Author(s) 2018
This work is subject to copyright. All rights are reserved by the Publisher, whether the whole or part of the material is concerned, specifically the rights of translation, reprinting, reuse of illustrations, recitation, broadcasting, reproduction on microfilms or in any other physical way, and transmission or information storage and retrieval, electronic adaptation, computer software, or by similar or dissimilar methodology now known or hereafter developed.
The use of general descriptive names, registered names, trademarks, service marks, etc. in this publication does not imply, even in the absence of a specific statement, that such names are exempt from the relevant protective laws and regulations and therefore free for general use.
The publisher, the authors and the editors are safe to assume that the advice and information in this book are believed to be true and accurate at the date of publication. Neither the publisher nor the authors or the editors give a warranty, express or implied, with respect to the material contained herein or for any errors or omissions that may have been made. The publisher remains neutral with regard to jurisdictional claims in published maps and institutional affiliations.

Printed on acid-free paper

This Springer imprint is published by Springer Nature
The registered company is Springer International Publishing AG
The registered company address is: Gewerbestrasse 11, 6330 Cham, Switzerland

Preface

Mass transfer from the gas phase to the solid phase is of interest in a broad range of applications. In order to accurately describe gas-to-particle mass transfer, a number of things must be known. These include the particle structure, thermal, fluid, and chemical conditions near the particle surface, and the flow condition—laminar, turbulent, etc. This introduces the importance of gas-to-particle mass transfer and the challenges posed in modeling the fluid-particle interactions, with an emphasis placed on the surface conditions and modeling the dynamics via direct numerical simulations (DNS) and large eddy simulations (LES). Subsequent chapters cover surface conditions and transport within the particle, model sorption kinetics and enhanced mass transfer, direct numerical simulation of mass transfer at different Stokes numbers, and the differences between DNS and LES in predicting gas-to-particle mass transfer. Additionally, the application of mercury adsorption on activated carbon is studied. Porous particles are modeled as a homogeneous assembly of sorbent material, forming a spherical, macroporous structure. The "Langmuir" theory is used to model sorption kinetics, and the effects of enhanced mass transfer due to convection at the gas/particle interface are captured.

This brief presents an integrated approach that includes the fluid-particle interactions in a manner that captures the underlying physicochemical interactions as a function of space and time. It incorporates recent developments in physical and mathematical modeling and numerical algorithms in one monograph and is divided into three chapters. Chapter 1 focuses on the fundamentals of gas-to-particle mass transfer (condensation and uptake), relevant parameters, and flow regimes. Chapter 2 introduces unsteady fluid motion and considers how those dynamics affect mass transfer. Finally, Chap. 3 discusses the application to turbulent flows (in the context of LES). We describe how such modeling is performed and the effects on the unresolved interactions on accuracy of the predictions.

This book introduces the latest information in the field; a conscious effort has been made to minimize coverage of related information that otherwise can be found in standard texts or technical references available in the open literature.

Minneapolis, MN, USA Sean C. Garrick
Minneapolis, MN, USA Michael Bühlmann
December 2016

Contents

1 Fundamentals of Gas-to-Particle Mass Transfer 1
  1.1 Introduction to Sorption Modeling 1
  1.2 Formulation 2
    1.2.1 Governing Equations 2
    1.2.2 Non-dimensionalization 4
  1.3 Problem Description 6
    1.3.1 Assumptions 6
    1.3.2 System Parameters 7
    1.3.3 Numerical Specifications 8
    1.3.4 Simulation Results for Concentration Fields and Gas-to-Particle Mass Transfer 8
    1.3.5 Analytical Solution for the Macropore Concentration in the Intermediate Regime 13
  1.4 Summary and Conclusions 14

2 Particle Dispersion and Mass Transfer in Turbulent Shear Flows 17
  2.1 Strategies for Sorption Modeling in Turbulent Flows 17
  2.2 Formulation 19
    2.2.1 Fluid Field 19
    2.2.2 Particle Field 19
    2.2.3 Gas-to-Particle Mass Transfer 20
  2.3 Particle Injection Through a Round Nozzle 21
    2.3.1 Particle Dispersion 21
    2.3.2 Particle Reynolds Number 23
  2.4 Multiphase Mixing Layer Transport 24
    2.4.1 Physical Parameters 25
    2.4.2 Numerical Specifications 26
    2.4.3 Fluid Field and Particle Dispersion 27
    2.4.4 Mass Transfer 30
  2.5 Summary and Conclusions 34

3 LES of Particle Dispersion and Gas-to-Particle Mass Transfer in Turbulent Shear Flows 37
3.1 Introduction 37
3.2 Formulation 38
  3.2.1 Fluid Field 38
  3.2.2 Particle Field 39
  3.2.3 Modeling of the SGS Stress 39
  3.2.4 Modeling of the SGS Fluid-Scalar Flux 41
3.3 Evaluation of SGS Closures for LES of Gas-to-Particle Mass Transfer 41
  3.3.1 Fluid Field 43
  3.3.2 Chemical Transport 46
  3.3.3 Performance Assessment 47
3.4 LES of Gas-to-Particle Mass Transfer 49
  3.4.1 Assumptions 49
  3.4.2 Numerical Specifications 50
  3.4.3 Fluid and Species Transport 50
  3.4.4 Particle Transport 52
  3.4.5 Mercury Adsorption 53
3.5 Summary and Conclusions 55

References 57

Acronyms

ACI	Activated carbon injection
DEV	Dynamic Smagorinsky eddy viscosity
DNS	Direct numerical simulation
LES	Large eddy simulation
MKEV	Modified kinetic energy eddy viscosity
PAC	Powder activated carbon
RANS	Reynolds averaged Navier-Stokes simulation
SEV	Smagorinsky eddy viscosity
SGS	Subgrid scale
SS	Scale similarity

Nomenclature

A	Surface mass transfer parameter
Bi_m	Mass transfer Biot number
c	Macropore concentration (kg/m^3)
C	Smagorinsky eddy viscosity model constant
C_k	Modified kinetic energy viscosity model constant
C_D	Dynamic eddy viscosity model coefficient
C_s	Similarity model coefficient
c_s	Concentration at particle surface (kg/m^3)
d_p	Particle diameter (m)
D_{eff}	Pore diffusivity (m^2/s)
D	Jet diameter (m)
f_p	Particle drag correction factor
g	Isotropic spatial filter
h_s	Spatial filter function
J_i	Scalar flux in the *i*-direction (m/s)
k_1	Adsorption rate coefficient
k_{mo}	External mass transfer coefficient
L_{ij}	Resolved subgrid-scale stress (m^2/s^2)
M_1	Mach number
M_{kl}	Modeled resolved subgrid-scale stress(m^2/s^2)
m_p	Particle mass (kg)
N_p	Number of particles
p	Fluid pressure (N/m^2)
q	Concentration in solid (kg/m^3)
$q_{\max}$	Maximum concentration in solid (kg/m^3)
Re_L	Flow Reynolds number
Re_p	Local particle Reynolds number
Re_{po}	Particle Reynolds number
Sc	Schmidt number
Sh	Sherwood number

S_{ij}	Rate of strain tensor (1/s)
Sc	Molecular Schmidt number
Sc_t	Subgrid-scale Schmidt number
St_K	Particle Stokes number
T	Fluid temperature (K)
t	Time (s)
T_{ij}	Test-filter stress
u_i	Velocity in the i-direction (m/s)
$u_i^\star$	Modified velocity in the i-direction (m/s)
$u_{i,p}$	Particle velocity in the i-direction (m/s)
U_1	Velocity of high-speed stream (m/s)
U_2	Velocity of co-flowing stream (m/s)
U_o	Characteristic or reference velocity (m/s)
x_i	Spatial coordinates (m)
$x_{i,p}$	Spatial location of particle in the i-direction (m)
Y_i	Mass fraction of species i
$\hat{\varDelta}$	Grid filter width (m)
$\overline{\varDelta}$	Test-filter width (m)
$\varDelta$	Grid spacing (m)
δ_{ij}	Kronecker delta
ϵ_p	Particle porosity
$\varGamma$	Species mass diffusion coefficient (m^2/s)
μ	Dynamic viscosity (kg/(m s))
ν_t	Subgrid-scale eddy viscosity (m^2/s)
ϕ	Scalar concentration (kg/m^3)
$\varPhi$	Thiele number
ρ	Fluid density (kg/m^3)
τ_{ij}	Subgrid-scale stress (m^2/s^2)
θ_j	Subgrid-scale fluid-scalar flux in the j-direction (m/s)
$\star$	Denotes nondimensional quantities
$\langle\rangle_L$	Spatial filtered variable

Chapter 1
Fundamentals of Gas-to-Particle Mass Transfer

Abstract Gas-to-particle mass transfer is studied analytically as well as numerically. Porous particles are modeled as a homogeneous assembly of sorbent material, forming a spherical, macroporous structure. The concentration in the macropores and in the solid is obtained as a function of time and space. The "Langmuir" theory is used to model sorption kinetics. Results show that, over a wide time range, the concentration in the solid is negligible, and the macropore concentration reaches a pseudo-steady state. For that case an analytical expression is derived for the macropore concentration inside the particle and at the particle surface in particular. It is shown that the surface concentration decreases with decreasing Biot numbers and increasing Thiele numbers. The analytical model discussed in this work can be utilized in computational mass transfer studies in lieu of the "perfect sink" assumption, in which the surface concentration is identically zero. Moreover, it captures the effects of enhanced mass transfer due to convection at the gas–particle interface.

1.1 Introduction to Sorption Modeling

Mass transfer from the gas phase to the solid phase is of interest in a broad range of applications, such as filtration, separation, purification, and catalytic reactions, among others [21, 30, 41, 83]. A practical example is the removal of mercury vapor—a by-product of coal-combusting processes—from incinerator flue gas. Historically, this was being done using fabric filters. A promising new technology is the injection of activated carbon particles directly into the flue gas, where the mercury vapor is adsorbed "in-flight" by particles, which are subsequently removed in an electrostatic precipitator (ESP) [17, 18, 68, 72, 97, 112]. Activated carbon is widely used to remove organic and inorganic contaminants from liquids and gases [88]. Its extensively developed internal pore structure and high surface-to-volume ratio give it an exceptionally high adsorption capacity [1, 31, 40]. In order to accurately describe gas–particle mass transfer, the surface conditions must be known. However, existing studies describe particles as perfect sinks (i.e., the surface concentration is identically zero) or rely on other restrictive assumptions such as a no-slip boundary condition. The perfect sink assumption leads to an overpredicted

S.C. Garrick, M. Bühlmann, *Modeling of Gas-to-Particle Mass Transfer in Turbulent Flows*, SpringerBriefs in Applied Sciences and Technology,
DOI 10.1007/978-3-319-59584-9_1

mass transfer rate—due to an unreasonably large concentration difference between the particle surface and the surrounding fluid—and the no-slip condition makes it impossible to account for convective effects at the gas–particle interface.

A comprehensive description of mass transfer from a moving fluid to porous particles accounts for convection, diffusion, and sorption kinetics. The latter has been studied extensively in recent years. Experiments have shown that sorption kinetics of adsorbents, such as activated carbon, can be described using the “Langmuir” theory [54]. Rate constants for the mass flux from the gas phase to the solid phase (adsorption) and in the opposite direction (desorption) have been determined for a variety of sorbents and flue gas compositions. It was found that doping the carbon particle surface with sulfur strongly increases the adsorption capacity [45, 46]. In other studies, where fly ash was used as sorbent, it was pointed out that sorption parameters significantly depend on temperature [47, 51, 53]. Several mathematical models have been proposed in the past to describe mass transfer and reaction kinetics inside porous catalysts. For particles with high porosity, the “homogeneous model” is valid, in which the catalyst is assumed to be an ensemble of small lumps of reactants distributed uniformly throughout the solid phase [43, 87]. In order to obtain an analytical solution, steady-state diffusion and first-order forward chemical reactions were assumed [5]. It has been shown that steady-state transport and reaction processes in porous catalysts are described by the Thiele number, incorporating reaction resistance and diffusion resistance [118]. Other researchers have studied mercury capture from incinerator flue gas by activated carbon injection [29, 97, 98]. The homogeneous model was used in combination with the Langmuir theory to describe the physical adsorption process. Those models were applied to several sorbents of practical use, such as raw and sulfur doped Darco® G60, Sorbalit®, and fly ash. It was found that very low utilization of the sorbent is achieved in the duct due to short particle flight times, whereas higher utilization is achieved with fabric filters, especially for long filtration times. A no-slip boundary condition was imposed at the particle surface. That is, particles are assumed to move at the speed of the surrounding fluid, and hence convective effects are neglected, although it is well known that convection increases mass transfer [39]. Gas–particle mass transfer in ESPs has also been studied under laminar and turbulent flow conditions [16–18]. Model results were based on the assumption that particles act as perfect mercury sinks. Consequently, mass transfer resistance associated with intra-particle diffusion and sorption kinetics was neglected.

1.2 Formulation

1.2.1 Governing Equations

Many adsorbents can be modeled as an assembly of microporous crystals, also referred to as “solid,” formed into a macroporous particle [29, 68, 87, 88, 91]. The transport equation for the macropore concentration is given by the porous media diffusion equation with an additional sink term representing mass transfer from the macropores to the solid:

$$\epsilon_p \frac{\partial c}{\partial t} = \epsilon_p \mathscr{D}_p \nabla^2 c - (1 - \epsilon_p) \frac{\partial q}{\partial t}, \tag{1.1}$$

where c is the concentration in the macropores, q is the concentration in the solid, ϵ_p is the particle porosity, and $\mathscr{D}_p$ is the macropore diffusivity, given by

$$\mathscr{D}_p = \epsilon_p \left(\frac{1}{\mathscr{D}} + \frac{1}{\mathscr{D}_{Kn}} \right)^{-1}. \tag{1.2}$$

If the mean pore diameter is much greater than the gas mean free path, mass transfer is governed by molecular diffusion, and Eq. (1.2) reduces to $\mathscr{D}_p = \epsilon_p \mathscr{D}$, where $\mathscr{D}$ is the molecular diffusion coefficient. In the limiting case of a pore diameter much smaller than the gas mean free path, however, mass transfer is due to Knudsen flow and Eq. (1.2) becomes $\mathscr{D}_p = \epsilon_p \mathscr{D}_{Kn}$, where $\mathscr{D}_{Kn}$ is the Knudsen diffusivity, given by

$$\mathscr{D}_{Kn} = d_{\text{pore}} \sqrt{\frac{8\hat{R}T}{9\pi M}}, \tag{1.3}$$

in which d_{pore} is the mean pore diameter, $\hat{R}$ is the universal gas constant, T is the gas temperature, and M is the molecular weight of the diffusing species [64, 97]. A zero-derivative boundary condition is applied to Eq. (1.1) at $r = 0$, where r is the radial coordinate, to account for the spherical symmetry of the particle:

$$\left. \frac{\partial c}{\partial r} \right|_{r=0} = 0. \tag{1.4}$$

The second boundary condition is obtained by flux matching at the particle surface. That is, the mass flux inside the particle at $r = d_p/2$ is equated with the mass flux from the surrounding fluid:

$$\epsilon_p \mathscr{D}_p \left. \frac{\partial c}{\partial r} \right|_{r=d_p/2} = k_m \Delta c_s, \tag{1.5}$$

where d_p is the particle diameter, k_m is the external mass transfer coefficient, and $\Delta c_s = c_\infty - c_s$ is the difference between the concentration in the surrounding fluid (outside the concentration boundary layer), c_∞, and the concentration at the particle surface, c_s [29, 83, 97–99]. In the context of this work, the Langmuir theory is most commonly used to describe the sorption process [22, 45–47, 53, 54, 68, 97, 98, 102, 119]. This model assumes that the sorption rate of adsorption is proportional to the concentration in the macropores, c, and the number of sites availablefor adsorption at the pore walls, $q_{\max} - q$; the rate of desorption is proportional to the number of already occupied sites, that is, the concentration in the solid, q. Consequently, the net sorption rate becomes

$$\frac{\partial q}{\partial t} = k_1 c(q_{\max} - q) - k_2 q, \tag{1.6}$$

where k_1 is the adsorption rate coefficient, k_2 is the desorption rate coefficient, and $q_{\max}$ is the maximum concentration in the solid in the limiting case of no desorption ($k_2 = 0\,\mathrm{s}^{-1}$). As time goes to infinity, a state of equilibrium ("saturation") is reached, and Eq. (1.6) yields the asymptotic value of the concentration in the solid as

$$q_\infty = q_{\max}\frac{c_\infty k_1}{c_\infty k_1 + k_2}. \tag{1.7}$$

1.2.2 Non-dimensionalization

The governing equations are nondimensionalized using appropriate reference quantities. This allows the results or dynamics observed to be of greater utility. In this context, the relevant quantities are length, time, and concentration:

$$r^\star = \frac{r}{L}, \quad t^\star = \frac{t}{t_o}, \quad c^\star = \frac{c}{c_o}, \quad q^\star = \frac{q}{q_o}. \tag{1.8}$$

Given the nature of spherically symmetric diffusion problems, the reference quantities are chosen to be

$$L = \frac{d_p}{2}, \quad t_o = \frac{L^2}{\mathscr{D}_p}, \quad c_o = c_\infty, \quad q_o = q_\infty, \tag{1.9}$$

where the reference length L is equal to the particle radius [29]. The reference time t_o takes into account the particle size and, through $\mathscr{D}_p$, the pore structure. The dimensionless time, $t^\star$, is also referred to as the Fourier number in the context of transient mass transfer. Asymptotic values are used to nondimensionalize concentrations, that is, $c^\star$ and $q^\star$ approach unity as $t^\star$ goes to infinity. With the relations from Eqs. (1.8) and (1.9), the nondimensional transport equations become

$$\frac{\partial c^\star}{\partial t^\star} = \nabla^{\star 2} c^\star - \frac{\alpha\beta}{\beta+\gamma}\frac{\partial q^\star}{\partial t^\star}, \tag{1.10}$$

and

$$\frac{\partial q^\star}{\partial t^\star} = c^\star(\beta+\gamma) - q^\star(c^\star\beta+\gamma), \tag{1.11}$$

in which α, β, and γ are given by

$$\alpha = \frac{q_{\max}(1-\epsilon_p)}{c_\infty \epsilon_p}, \quad \beta = \frac{k_1 c_\infty (d_p/2)^2}{\mathscr{D}_p}, \quad \gamma = \frac{k_2 (d_p/2)^2}{\mathscr{D}_p}, \tag{1.12}$$

where α represents the mass ratio of species in the solid to species in the macropores at equilibrium, and β and γ are the nondimensional adsorption and desorption rate coefficients, respectively. The square root of the dimensionless group $\alpha \times \beta$ is referred to as the Thiele number:

$$\varPhi = \sqrt{\alpha \times \beta} = \sqrt{\frac{q_{\max}(1-\epsilon_p) k_1 (d_p/2)^2}{\epsilon_p \mathscr{D}_p}}. \tag{1.13}$$

The Thiele number is the ratio of the adsorption rate at the pore walls to the diffusive mass transfer rate inside the macropores [83, 110, 118]. For $\varPhi \gg 1$ the adsorption rate is much larger than the diffusion rate. Therefore, the diffusing species is likely to be adsorbed before it can penetrate far into the macropores. For $\varPhi \ll 1$ the adsorption rate is small compared to the diffusion rate, and the macropore concentration becomes more uniform. The boundary conditions for Eq. (1.10) become

$$\left.\frac{\partial c^\star}{\partial r^\star}\right|_{r^\star=0} = 0, \quad \left.\frac{\partial c^\star}{\partial r^\star}\right|_{r^\star=1} = Bi_m \Delta c_s^\star, \tag{1.14}$$

where Bi_m is the Biot number in mass transfer, given by

$$Bi_m = \frac{k_m d_p/2}{\epsilon_p \mathscr{D}_p} = \frac{Sh \mathscr{D}}{2\epsilon_p \mathscr{D}_p}, \tag{1.15}$$

in which Sh is the Sherwood number, defined as

$$Sh = \frac{k_m d_p}{\mathscr{D}}. \tag{1.16}$$

In analogy to the Biot number in heat transfer, Bi_m is defined as the ratio of the mass transfer rate at the fluid–particle interface to the diffusive mass transfer rate inside the macropores [4, 29, 68]. Values of Bi_m that are much smaller than unity imply that the concentration gradient in the surrounding fluid, $\Delta c_s^\star = 1 - c_s^\star$, is much larger than the concentration gradient inside the particle. Consequently, concentration gradients inside the particle are negligible for $Bi \ll 1$, and a lumped system approach is reasonable. The Sherwood number is the ratio of the mass transfer rate at the fluid–particle interface to the diffusive mass transfer rate in the fluid. It is generally a function of the Reynolds number (the ratio of inertia to viscous forces) and the Schmidt number (the ratio of momentum to mass diffusivities) [32]. As such, it captures the effects of the flow field on the mass transfer to the particle.

In the limiting case of small, spherical particles, providing no relative velocity at the gas–particle interface, the Sherwood number approaches a value of $Sh = 2$ [72]. For a moving fluid, however, the Sherwood number increases and thereby accounts for enhanced external mass transfer due to convective effects [16–18, 29, 68, 86, 103].

1.3 Problem Description

The mass transfer process under consideration is a quasi-one-dimensional convection/diffusion/sorption problem. A single porous particle is considered suspended in a fluid containing a species at concentration c_∞. The mass transfer process is comprised of three parts: (1) condensation of vapor molecules toward the particle surface through convection and diffusion, (2) pore diffusion inside the particle, and (3) adsorption to the solid structure of the particle. Figure 1.1 illustrates such a process schematically.

1.3.1 Assumptions

It is assumed that particles are spherical in shape with a homogeneous, porous structure. The particle diameter is much larger than the gas mean free path. Mass transport through the solid (micropore diffusion) is neglected, that is, macropore diffusion is the dominant mass transfer process and obeys Fick's law [66, 88]. The surrounding medium is assumed to be "infinite," that is, c_∞ is constant. No phase change is involved in the isothermal mass transport process; only gaseous diffusion inside the pore network is considered [97].

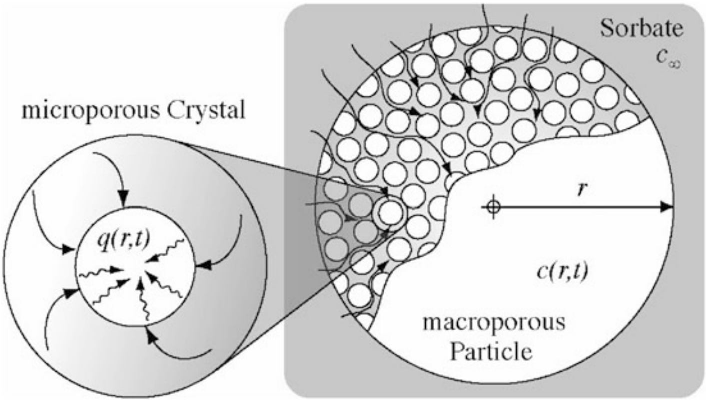

Fig. 1.1 Macroporous particle, modeled as an assembly of microporous crystals

1.3.2 System Parameters

Six parameter sets (cases 1–6) will be used to exemplify the species concentration inside the particle and the gas–particle mass transfer associated with it. The first two cases stem from investigations in which carbon particles have been used as sorbent material to remove mercury vapor from gas. Parameters for cases 3–6 are varied systematically, starting from case 2. The sole purpose of case 1 is to verify the consistency of the simulation results by comparison with existing data. To this end we adopt parameters from [97]. That study includes a variety of sorbent materials under different operating conditions. Case 1 represents Darco® G60 carbon blacks with diameter $d_p = 20\,\mu\text{m}$. The carrier gas is oxygen (O_2) at a temperature of $T = 423.15\,\text{K}$ containing trace amounts of mercuric chloride ($HgCl_2$). Case 2 represents typical operating conditions of an ESP. Temperature, mercury species, concentration in the fluid, and particle density are chosen in accordance with [17]. Sorption parameters for Darco® G60 carbon blacks are extrapolated to a temperature of $T = 500\,\text{K}$ from data given by Karatza et al. [46]. The molecular diffusivity of elemental mercury (Hg) in nitrogen (N_2) is calculated with an expression for dilute gases given by Slattery and Bird [104]. Cases 3–6 are derived from case 2 by separately changing the governing parameters α, β, γ, and Bi_m. In case 3, the Biot number is reduced to $Bi_m = 0.1$. In case 4, the parameter α is increased by a factor 100 with respect to case 2. Whereas in case 5, the parameters β and γ are increased by a factor 100 with respect to case 2. Both changes do not affect the Biot number but result in a Thiele number of $\Phi = 4.331$. Case 6 is a combination of cases 3 and 5 in that the parameters β, γ, and Bi_m are changed at the same time. Nondimensional simulation parameters for all cases are summarized in Table 1.1.

Table 1.1 Intra-particle diffusion, sorption kinetics, and gas–particle mass transfer: simulation parameters and results

	Case 1	Case 2	Case 3	Case 4	Case 5	Case 6
α	8.93×10^{7}	7.10×10^{8}	7.10×10^{8}	7.10×10^{10}	7.10×10^{8}	7.10×10^{8}
β	1.55×10^{-8}	2.64×10^{-10}	2.64×10^{-10}	2.64×10^{-10}	2.64×10^{-8}	2.64×10^{-8}
γ	6.51×10^{-8}	3.39×10^{-8}	3.39×10^{-8}	3.39×10^{-8}	3.39×10^{-6}	3.39×10^{-6}
Bi_m	38.15	208.42	0.1	208.42	208.42	0.1
Φ	1.1765	0.4331	0.4331	4.331	4.331	4.331
$\underset{\sim}{\tau}^{\star}_{\mathrm{srpt}}$	1.25×10^{5}	2.93×10^{5}	4.73×10^{5}	2.97×10^{5}	2.97×10^{3}	1.00×10^{5}
$\dot{m}^{\star}_{p}$	7.32×10^{-8}	3.37×10^{-8}	2.08×10^{-8}	1.79×10^{-8}	1.79×10^{-6}	5.30×10^{-8}
$\tilde{c}^{\star}_{s}$	0.9890150	0.9997038	0.6182060	0.9842623	0.9842623	0.0291329
$\Delta\tilde{c}^{\star}_{s}$	1.10×10^{-2}	2.96×10^{-4}	3.82×10^{-1}	1.57×10^{-2}	1.57×10^{-2}	9.71×10^{-1}

1.3.3 Numerical Specifications

The numerical algorithm used allows to solve for the concentration in the macropores, $c^\star$, and the concentration in the solid, $q^\star$, as a function of time, $t^\star$, and space, $r^\star$. The governing equations are solved in nondimensional form using the Crank–Nicolson difference scheme [109]. This implicit scheme is unconditionally stable and second-order accurate in time and space. Second-order accurate boundary conditions are imposed at the center of the particle and at the surface. The computational grid is evenly spaced and is comprised of 501 grid points. The resolution in time and space was chosen such that large gradients at the particle surface are resolved sufficiently accurate.

1.3.4 Simulation Results for Concentration Fields and Gas-to-Particle Mass Transfer

The temporal evolution of the macropore concentration, $c^\star$, as a function of the radius, $r^\star$, is shown in Fig. 1.2. The concentration is obtained for case 1 where $t_o = 1.55 \times 10^{-4}$ s. The results show that, after the particle is introduced into a medium with concentration $c^\star_\infty = 1$, the macropore concentration increases from an initial value of $c^\star = 0$ to a final value of $c^\star = 1$ at $t^\star = 10^8$ (or $t = 4.3\,\text{h}$). As mass diffuses into the macropores, the concentration increases throughout the particle. At time $t^\star = 1$ the macropore concentration in the center of the particle has reached a value of $c^\star = 0.79$. This is in good agreement with results by Scala [97]. At time $t^\star = 10^8$ the concentration gradient vanishes, and mass transfer comes to a halt. The particle is saturated.

The macropore concentration, $c^\star$, and the concentration in the solid, $q^\star$, as a function of time, $t^\star$, on a logarithmic scale are shown in Fig. 1.3. Four curves are shown representing $c^\star$ and $q^\star$ at the particle center ($r^\star = 0$) and at the surface ($r^\star = 1$), obtained in case 1. The macropore concentration at the particle surface

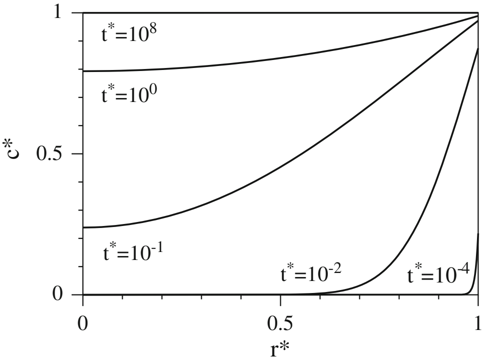

Fig. 1.2 Macropore concentration, $c^\star$, as a function of the radial coordinate, $r^\star$, at time $t^\star = 10^{-4}$, $t^\star = 10^{-2}$, $t^\star = 10^{-1}$, $t^\star = 10^0$, and $t^\star = 10^8$, obtained in case 1

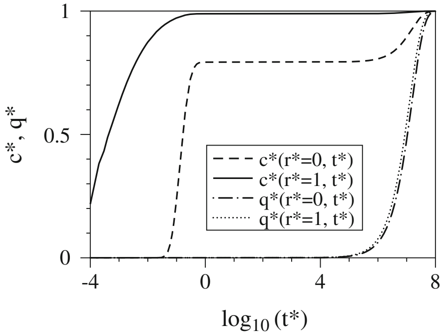

Fig. 1.3 Temporal evolution of the macropore concentration, $c^\star$, and the concentration in the solid, $q^\star$, at the particle center ($r^\star = 0$) and at the surface ($r^\star = 1$), obtained in case 1

increases steadily until time $t^\star = 1$. At the center of the particle, the macropore concentration starts to increase at time $t^\star = 0.01$. In the time range $1 < t^\star < 10^5$, the macropore concentration at the surface remains at a value 98.9% that of the environment ($c^\star = 0.989$), the macropore concentration at the particle center has a constant value of $c^\star = 0.79$, and the concentration in the solid is negligibly small ($q^\star < 0.01$). The concentration in the solid increases from a value of $q^\star = 0.01$ at time $t^\star = 10^5$ to its final value of $q^\star = 1$ at time $t^\star = 10^8$. This concentration increase in the solid phase triggers a further increase of the macropore concentration to its asymptotic value $c^\star_\infty = 1$. Hence, the mass transfer process can be divided into three different phases. After the particle surface is subjected to a step change in concentration, the condensable species diffuses into the macropores. Mass transfer is due to macroporous diffusion. We refer to this first phase as the "diffusion regime." As the concentration in the macropores increases, vapor molecules begin to adsorb to the pore walls. Ultimately, the diffusional mass flux in the gas phase (inside the macropores) is balanced by the gas-to-solid mass flux (adsorption), and the macropore concentration does not change with time. We call this second phase "intermediate regime." As more and more molecules are deposited on the pore walls, the concentration in the solid increases. In the third phase, the "sorption regime," the concentration in the solid increases from a value of less than $q^\star = 0.01$ to its final value of $q^\star = 1$. Figure 1.3 reveals that the diffusion regime ends at time $t^\star = 1$, the intermediate regime spans over the time range $1 < t^\star < 10^5$, and the sorption regime ranges from time $t^\star = 10^5$ to $t^\star = 10^8$. These time ranges are not universal, however, and can differ for other parameter sets.

A more complete view is shown in Fig. 1.4. The contours in Fig. 1.4 show the macropore concentration, $c^\star$, as a continuous function of time and space for cases 1–6. The radial coordinate, $r^\star$, is shown on the abscissa, and time, $t^\star$, is shown on the logarithmic ordinate. The temporal evolution of $c^\star$, as shown in Figs. 1.2 and 1.3 for case 1, corresponds to slices of Fig. 1.4a at given times and radial locations. The results for case 2 are shown in Fig. 1.4b. As in case 1, the largest gradients across the particle are observed in the diffusion regime ($t^\star < 1$). The macropore concentration reaches a plateau in the intermediate regime ($1 < t^\star < 10^5$), before it increases again in the sorption regime ($t^\star > 10^5$). Figure 1.4c and f illustrate the

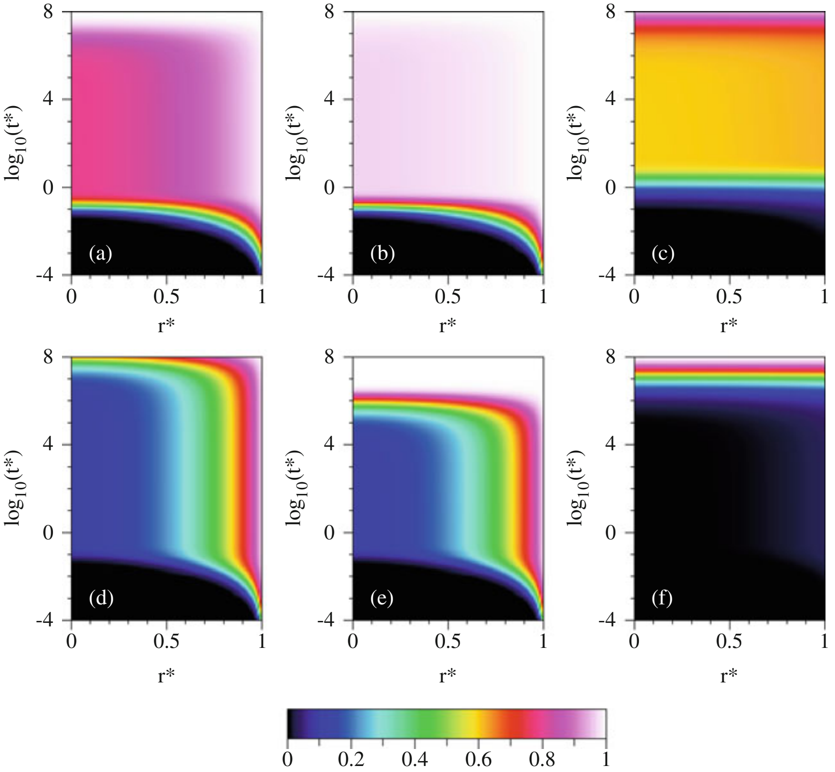

Fig. 1.4 Macropore concentration, $c^{\star}$, as a function of the radial coordinate, $r^{\star}$, and time, $t^{\star}$: (**a**) case 1; (**b**) case 2; (**c**) case 3; (**d**) case 4; (**e**) case 5; (**f**) case 6

concentration fields of cases 3 and 6, respectively. Both cases can be considered lumped due to a mass Biot number much less than unity ($Bi_m = 0.1$). As a result, the macropore concentration does not vary significantly with radius, $r^{\star}$. A lumped analysis yields the macropore concentration in the intermediate regime as

$$c^{\star}_{lmp} = \left(1 + \frac{\Phi^2}{3Bi_m}\right)^{-1}. \tag{1.17}$$

Both cases 3 and 6 have the same mass Biot number. Hence, it is the larger Thiele number which causes the smaller macropore concentration in case 6. Cases 4 and 5 are shown in Fig. 1.4d, e, respectively. Large concentration gradients across the particle are observed in the intermediate regime in both cases. This is due to a large Thiele number, corresponding to high adsorption rates. Case 5 differs from case 4 in that the adsorption and desorption rate coefficients, β and γ, are larger, and thus the particle is saturated earlier (at time $t^{\star} = 10^7$).

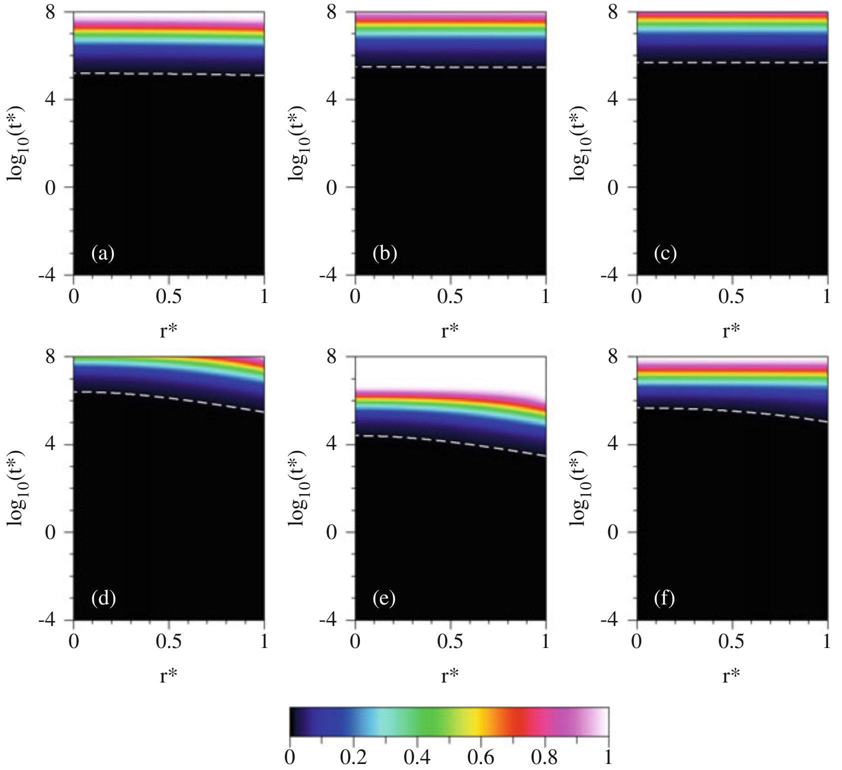

Fig. 1.5 Concentration in the solid, $q^\star$, as a function of the radial coordinate, $r^\star$, and time, $t^\star$: (**a**) case 1; (**b**) case 2; (**c**) case 3; (**d**) case 4; (**e**) case 5; (**f**) case 6

The concentration in the solid, $q^\star$, is presented in a similar fashion in Fig. 1.5. The white dashed line represents a concentration of $q^\star = 0.01$. All cases have this in common—the concentration in the solid is negligible ($q^\star < 0.01$) in the diffusion and intermediate regime. In general, $q^\star$ can be considered lumped. However, gradients across the particle are observed in cases 4–6 caused by large Thiele numbers ($\Phi = 4.331$). Figure 1.5e reveals that the sorption regime starts at $t^\star = 10^3$ in case 5. In all other cases, the sorption regime starts at $t^\star = 10^5$. With the conclusion that $q^\star$ is much smaller than $c^\star$ outside the sorption regime, the transport equations simplify in the diffusion regime and intermediate regime to

$$\frac{\partial c^\star}{\partial t^\star} = \nabla^2 c^\star - \Phi^2 c^\star \tag{1.18}$$

and

$$\frac{\partial q^\star}{\partial t^\star} = (\beta + \gamma)\, c^\star. \tag{1.19}$$

It should be noted that Eq. (1.18) is now decoupled from Eq. (1.19), and the sorption rate is only a function of the macropore concentration, $c^\star$. That is, the mass transfer from the macropores to the solid phase is essentially a “forward reaction.” Equation (1.19) reveals that, in the intermediate regime, where the macropore concentration is constant, the concentration in the solid increases linearly with time at a rate of $(\beta+\gamma)\tilde{c}^\star$. (Constant quantities in the intermediate regime are henceforth denoted by $\sim$.) Thus, the concentration in the solid reaches a value of 1% of its final value at time:

$$\tau^\star_{\mathrm{srpt}} \approx \frac{0.01}{(\beta+\gamma)\tilde{c}^\star}. \tag{1.20}$$

The sorption time scale, $\tau^\star_{\mathrm{srpt}}$, marks the beginning of the sorption regime. Since $\tilde{c}^\star$ is in general a function of radius, $\tau^\star_{\mathrm{srpt}}$ varies based on what value of $\tilde{c}^\star$ is considered. Values for the sorption time scale are listed in Table 1.1, where the surface macropore concentration in the intermediate regime, $\tilde{c}^\star_s$, is used for $\tilde{c}^\star$ in Eq. (1.20). It is confirmed that the sorption time scale in case 5 is two orders of magnitude smaller as compared to the other cases.

The mass growth rate of the particle, $\dot{m}^\star_p$, is given by

$$\dot{m}^\star_p = \frac{dm^\star_p}{dt^\star} = \frac{3Bi_m}{\Phi^2}(\beta+\gamma)\Delta c^\star_s, \tag{1.21}$$

where $m^\star_p$ is the mass of species deposited on the particle, normalized by the maximum mass uptake capacity. The temporal evolution of the mass of species deposited on the particle, $m^\star_p$, is shown in Fig. 1.6 for all cases. Six curves are obtained from simulation results by numerically integrating Eq. (1.21). Because the mass is normalized by the maximum uptake capacity, all curves approach a value of $m^\star_p = 1$ as time goes to infinity. Three distinct regions are identifiable:

Fig. 1.6 Temporal evolution of the mass of species deposited on the particle, $m^\star_p$

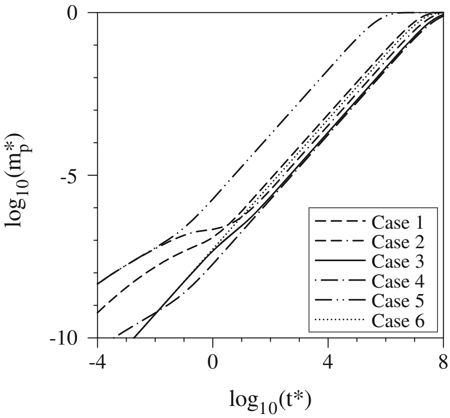

in the intermediate regime, the particle mass grows linearly with time. Values for the constant particle mass growth rate in the intermediate regime, denoted by $\widetilde{\dot{m}_p^\star}$, are listed in Table 1.1. In the diffusion regime, where the concentration difference at the surface, $\Delta c_s^\star$, is greater than in the intermediate regime, growth rates are larger than $\widetilde{\dot{m}_p^\star}$. Conversely, growth rates decrease in the sorption regime. As it was pointed out earlier, the transition between the diffusion regime, intermediate regime, and sorption regime is not always clear and differs from case to case. However, Fig. 1.6 reveals that, in general, the diffusion regime ends at time $t^\star = 1$, and the intermediate regime spans from time $t^\star = 1$ to $t^\star = 10^5$.

1.3.5 Analytical Solution for the Macropore Concentration in the Intermediate Regime

Figure 1.4 reveals that, in all cases, the macropore concentration does not change with time in the intermediate regime. This allows the derivation of an analytical expression for the macropore concentration in the intermediate regime, $\tilde{c}^\star$. The solution of Eq. (1.18), assuming a steady state ($\partial c^\star / \partial t^\star = 0$), and subject to boundary conditions as specified in Eq. (1.14), is

$$\tilde{c}^\star = \frac{C_1}{\sqrt{r^\star}} I_{1/2} \left(\Phi r^\star \right), \tag{1.22}$$

where C_1 is a constant, given by

$$C_1 = \frac{Bi_m}{\Phi I_{3/2} \left(\Phi \right) + Bi_m I_{1/2} \left(\Phi \right)}, \tag{1.23}$$

and $I_v(x)$ is the modified Bessel function of the first kind of order v. In particular, the constant surface concentration in the intermediate regime becomes

$$\tilde{c}_s^\star = C_1 I_{1/2} \left(\Phi \right) = \frac{Bi_m}{Bi_m + \Phi / \tanh(\Phi) - 1}. \tag{1.24}$$

Equations (1.22)–(1.24) are consistent with results previously obtained by other researchers [5, 43, 118]. Figure 1.7 shows the surface concentration in the intermediate regime, $\tilde{c}_s^\star$, plotted as a function of the Thiele number, Φ, and the Biot number, Bi_m, on a logarithmic scale. The surface concentration approaches unity with decreasing Thiele numbers and increasing Biot numbers. However, for $\Phi = 10$ and $Bi_m = 0.1$, for example, the surface concentration almost vanishes, that is, the particle acts as a perfect sink. The locations of cases 1–6 are shown in the Φ–Bi_m-plane. Values for $\tilde{c}_s^\star$ are listed in Table 1.1 as well. In cases 1–5, the surface concentration is greater than $\tilde{c}_s^\star = 0.98$. In case 3, the surface concentration is $\tilde{c}_s^\star = 0.62$. Case 6 is an example of a perfect sink; the surface concentration is $\tilde{c}_s^\star = 0.03$.

Fig. 1.7 Analytical solution for the surface concentration in the intermediate regime, $\tilde{c}_s^\star$, in the range of $0.1 \leq \Phi \leq 10$ and $0.01 \leq Bi_m \leq 1000$

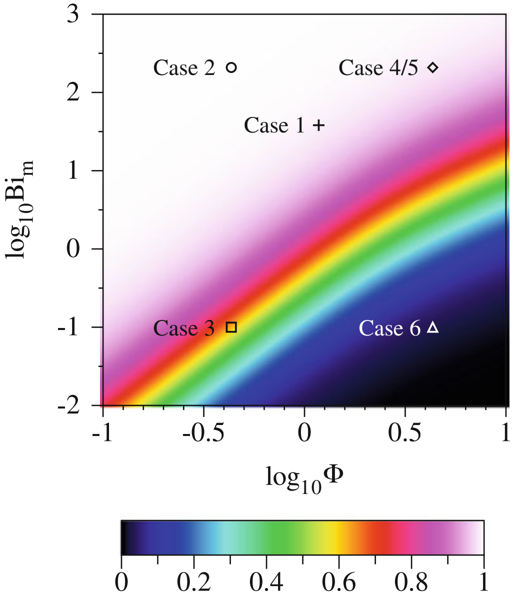

The concentration difference between the particle surface and the surrounding fluid is the "driving force" for mass transfer. Equation (1.24) reveals that, in the intermediate regime, the concentration difference, $\Delta\tilde{c}_s^\star = 1 - \tilde{c}_s^\star$, is only a function of the Thiele number and the Biot number. Values for $\Delta\tilde{c}_s^\star$ are listed in Table 1.1 as well. The effect of the Thiele number on $\Delta\tilde{c}_s^\star$ at constant Biot numbers is revealed in Fig. 1.8a. Three curves are obtained for Biot numbers $Bi_m = 0.1$ (cases 3 and 4), $Bi_m = 38.15$ (case 1), and $Bi_m = 208.42$ (cases 2, 4, and 5). Conversely, Fig. 1.8b shows the effect of the Biot number on $\Delta\tilde{c}_s^\star$ for constant Thiele numbers: $\Phi = 0.4331$ (cases 2 and 3), $\Phi = 1.1765$ (case 1), and $\Phi = 4.331$ (cases 4–6). It is revealed that the concentration difference at the particle surface increases with increasing Thiele numbers and decreasing Biot numbers.

1.4 Summary and Conclusions

Gas-to-particle mass transfer is studied numerically and analytically. A single porous particle was modeled as a homogeneous assembly of sorbent material, forming a spherical macroporous structure. The Langmuir theory was utilized to describe mass transfer from the macropores to the solid. The concentration in macropores and in the solid was obtained as a function of time and space by solving the porous media diffusion equation numerically. Simulations were performed for six different sets of the governing parameters.

Fig. 1.8 Concentration difference in the intermediate regime, $\Delta\tilde{c}_s^\star$, as a function of (**a**) the Thiele number, Φ, and (**b**) the Biot number, Bi_m

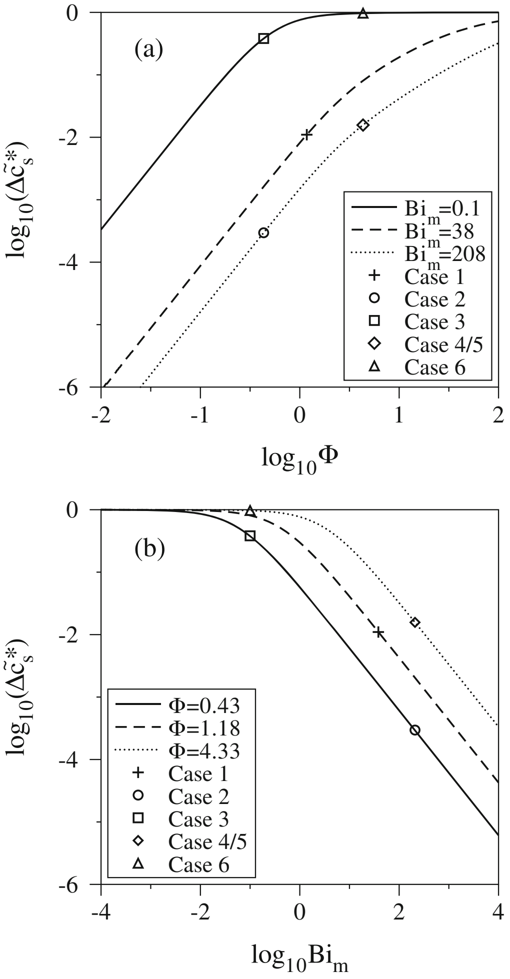

The results revealed that the mass transfer process can be divided into three phases: we termed these the diffusion, intermediate, and sorption regimes. The concentration in the solid is negligible in the first two phases, and the concentration in the macropores reaches a quasi- steady state in the intermediate regime. An analytical solution for the macropore concentration in the intermediate regime was derived, providing a two-parameter model for the surface concentration, which takes into account the sorption characteristics of the particle—through the Thiele number—and captures nontrivial flow conditions at the gas–particle interface through the mass Biot number. It was shown that the surface concentration in the intermediate regime decreases with decreasing mass Biot numbers and increasing Thiele numbers. However, the model is limited to an intermediate time range in which intra-particle diffusion reaches a pseudo-steady state, and the local adsorption rate depends on the macropore concentration only. Nevertheless, it provides an estimate for the surface concentration superior to the perfect sink assumption and can be used for gas–particle mass transfer simulations in complex flows where it is computationally unfeasible to solve an additional transport equation inside every single particle.

Studies of mercury removal from flue gas have revealed the need to know the species concentration at the particle surface. The model presented in this work can be used for gas–particle mass transfer simulations in complex flows where it is computationally unfeasible to solve an additional transport equation inside every single particle. It takes into account the sorption characteristics of the particle and captures nontrivial flow conditions at the gas–particle interface. However, it is limited to an intermediate time range in which intra-particle diffusion reaches a pseudo-steady state, and the local adsorption rate only depends on the macropore concentration. Nevertheless, it provides an estimate for the surface concentration superior to the perfect sink assumption.

Chapter 2
Particle Dispersion and Mass Transfer in Turbulent Shear Flows

Abstract DNS of condensation mass transfer in particle-laden incompressible turbulent mixing layers are performed. The flows are comprised of a particle-free condensable vapor mixing with micron-size porous particles. Simulations are performed at a single Reynolds number while varying the particle Stokes number, the mass transfer and convective time scales, and the vapor concentration at the particle surface. Convection-enhanced mass transfer and the surface concentration at the gas/particle interface are of great importance in accurately predicting gas–particle mass transfer rates. Particle slip velocities are varied by considering different particle Stokes numbers. Simulations utilizing the "perfect sink" assumption are compared with simulations in which the non-zero, steady-state surface concentration is calculated taking into account the sorption properties of porous particles. Results indicate that particle dispersion is greater at lower particle Stokes numbers. However the increased particle slip velocity in the higher particle Stokes number flows result in increased condensation. Furthermore, results show that the perfect sink assumption leads to an overprediction in the condensation mass transfer rate.

2.1 Strategies for Sorption Modeling in Turbulent Flows

Gas-to-particle mass transfer in turbulent flows is not very well understood. Little physical data is available from full-scale tests. Numerical simulation of condensation mass transfer in turbulent particle-laden flows can improve our understanding of the underlying dynamics and transport processes as well as provide useful knowledge and guidance in the design and performance of the so-called virtual sorbent beds.

A large number of computational studies of condensation mass transfer rely on assumptions which are rather restrictive, or questionable, when made, or applied, in the context of turbulent flows. One such assumption concerns the vapor/gas concentration at the particle surface. The perfect sink assumption, for instance, implies that the concentration of condensable vapor at the particle surface is identically zero [16–18]. Consequently, mass transfer resistances associated with intra-particle diffusion and sorption kinetics are neglected. For that matter, the

S.C. Garrick, M. Bühlmann, *Modeling of Gas-to-Particle Mass Transfer in Turbulent Flows*, SpringerBriefs in Applied Sciences and Technology,
DOI 10.1007/978-3-319-59584-9_2

vapor concentration at the fluid–particle interface is of critical importance. An analytical expression for the concentration may be obtained under the assumption of steady-state pore diffusion [5, 43, 88, 118]. These expressions are valid over a wide time range and remove the need to solve the species transport equation within the particles. Of great concern is the physics/dynamics at the fluid–particle interface. From a flow physics perspective, the mass transfer depends on the fluid velocity at the particle surface. Research has shown that the gas–particle slip velocity grows linearly with the particle Stokes number [95]. More specifically, researchers have identified regions of positive and negative slip velocities related to accelerating and decelerating fluid regions, respectively [49, 73]. Although the presence of the particle slip velocity enhances mass transfer rates [32, 39, 81, 82, 120], it has been neglected in several studies [29, 72, 97–99]. The presence of fluctuating scalar/chemical and particle fields in turbulent flows, and the resultant variation in residence times, suggests that modeling of the temporally and spatially varying fluid–particle dynamics would improve our predictive ability [13, 18, 24, 99, 116].

Particle dispersion in turbulent flows has been studied extensively in the past several decades [3, 10, 11, 52, 55, 61, 68, 74, 76, 77, 107, 111, 115]. DNS was used to investigate the effect of isotropic turbulence on the particle concentration and identify flow regions that significantly influence particle transport and mixing [107]. The computational expense of DNS renders it prohibitive for simulation of practical flows. Methods such as LES and RANS are commonly used to model fluid flow in more complex geometries [3, 52, 68, 89, 111]. In performing LES or RANS, only the large-scale or mean fluid motion is resolved, and the effects of the small-scale fluctuations on particle dispersion and condensation are largely unknown [38, 80]. Good agreement was found between experiments and DNS of inertial particle clustering in a three-dimensional, isotropic turbulence field, suggesting that three-dimensional simulations are needed to accurately describe particle motion in turbulent flows [92]. It has been reported that the use of LES may result in significant errors in predicting particle motion for Stokes numbers around unity [74]. Additionally, modeling efforts of particle-laden flows with condensation have thus far neglected the effects of turbulence on condensation or have been otherwise un-validated [68].

We consider the condensation of vapor onto micron-size particles in turbulent mixing layers. The motivation is twofold: to elucidate the effects of different flow/particle parameters on condensation mass transfer in turbulent flows and to establish datasets that may be used in evaluating the performance of turbulence models (in the contexts of LES and RANS). Several nondimensional parameters are varied to consider the effects of (1) the “driving” force or concentration difference between the particle, and the fluid is varied, (2) mass transfer across the particle, and (3) particle dispersion on condensation mass transfer.

2.2 Formulation

2.2.1 Fluid Field

The flows under consideration are described by the incompressible Navier–Stokes equations. The primary transport variables are the fluid velocity, u_i, and the fluid pressure, p. These variables are governed by the conservation of mass and momentum equations

$$\frac{\partial u_j}{\partial x_j} = 0, \tag{2.1}$$

$$\frac{\partial u_i}{\partial t} + \frac{\partial u_i u_j}{\partial x_j} = -\frac{\partial p}{\partial x_i} + \frac{1}{Re_L}\frac{\partial^2 u_i}{\partial x_j \partial x_j}, \tag{2.2}$$

where Re_L is the Reynolds number. The transport of a condensable vapor is given by

$$\frac{\partial Y_i}{\partial t} + \frac{\partial u_j Y_i}{\partial x_j} = \frac{1}{Re_L Sc}\frac{\partial^2 Y_i}{\partial x_j \partial x_j}, \tag{2.3}$$

where Y_i is the mass fraction of species i and Sc is the Schmidt number.

2.2.2 Particle Field

The equations describing the particle trajectories are

$$\frac{dx_{i,p}}{dt} = u_{i,p}, \qquad \frac{du_{i,p}}{dt} = \frac{f_p}{St_k}(u_i - u_{i,p}) \tag{2.4}$$

where $x_{i,p}$ is the particle location, $u_{i,p}$ is the particle velocity in the x_i direction, f_p is the drag correction factor,

$$St_k = \frac{d_p^2 \rho_p}{18\,\mu} \times \frac{U_o}{L} \tag{2.5}$$

is the particle Stokes number, d_p is the particle diameter, ρ_p is the particle bulk density, μ is the dynamic fluid viscosity, L is the reference length, and U_o is the reference velocity [3, 30, 61, 76, 78]. The drag correction factor, f_p, accounts for increased drag in the outer Stokesian region due to vortex shedding in the wake of the particle and is given by

$$f_p = 1 + 0.15 Re_p^{0.687}, \tag{2.6}$$

where $Re_p = |\Delta u_i| Re_{po}$ is the particle Reynolds number and $Re_{po} = d_p U_o/\nu$, where ν is the kinematic viscosity [41]. The ratio St_k/f_p is also referred to as a nondimensional particle relaxation time, describing the ability of a particle to adjust to the surrounding fluid [3]. Buoyancy forces, added mass effects, and Basset forces are neglected, as well as pressure gradients and shear forces across the length of the particles [55]. The particle volume fraction and mass loadings are assumed to be sufficiently low to neglect particle–particle interactions; the dynamics of the flow are not modified by the presence of particles [76, 77]. All particles are assumed rigid spheres, the diameter of which is much larger than the gas mean free path.

2.2.3 Gas-to-Particle Mass Transfer

The condensable vapor is transferred from the fluid to the particle surface by convection and diffusion. The particle mass growth rate is equal to the mass flow rate toward a single particle and is given by

$$\frac{dm_p}{dt} = A\frac{Sh}{2}Y(1 - c_s), \tag{2.7}$$

where m_p is the particle mass (nondimensionalized by the mass of vapor initially contained in volume L^3), Sh is the Sherwood number, c_s is the vapor concentration at the particle surface, and the parameter A is given by $A = (k_{mo} d_p^2 \pi)/(U_o L^2)$, in which k_{mo} is the external mass transfer coefficient in a quiescent fluid. The parameter A represents the ratio of diffusive mass transfer to the particle surface and advective mass transfer in the bulk flow. It is the product of a dimensionless velocity, k_{mo}/U_o, and a dimensionless area, $d_p^2\pi/L^2$, and can be written in terms of nondimensional groups as $A = (2\pi Re_{po})/(Sc Re_L^2)$. For $A \ll 1$ advection is the dominant mode of mass transfer in the particle-laden flow. The Sherwood number is the ratio of the mass transfer rate at the fluid–particle interface to the diffusive mass transfer rate in the fluid and accounts for the increased mass transfer due to convective effects at the particle surface. The augmentation in mass transfer is due to the presence of a particle slip velocity. We adopt a semiempirical correlation for Sh, first proposed by Frössling [32], who showed analytically that the Sherwood number is proportional to $Re_p^{1/2} Sc^{1/3}$:

$$Sh = 2 + 0.552 Re_p^{1/2} Sc^{1/3}, \tag{2.8}$$

The expression was developed using experimental data for evaporating drops and was later used in the context of gas–particle mass transfer [17, 18, 29, 68]. If the particle is treated as a perfect sink, the surface concentration vanishes (that is, $c_s = 0$). Conversely, if the vapor concentration at the particle surface is equal to the vapor concentration in the surrounding fluid, c_s is equal to unity, and there is no mass transfer. For the case where neither assumption is valid, the concentration at the surface is given by

$$c_s = \frac{Bi_m}{Bi_m + \Phi / \tanh \Phi - 1}, \quad \Phi = \sqrt{\frac{q_{\max}(1 - \epsilon_p) k_1 (d_p/2)^2}{\mathscr{D}_{\text{eff}}}}, \tag{2.9}$$

where Φ is the Thiele number, $Bi_m = Bi_{mo}Sh/2$ is the Biot number for mass transfer, $Bi_{mo} = (k_{mo}d_p/2)/\mathscr{D}_{\text{eff}}$ is the reference mass Biot number, and $\mathscr{D}_{\text{eff}}$ is the effective pore diffusivity [5, 43, 72, 83, 97, 110, 118]. The mass Biot number is the ratio of the mass transfer rate at the fluid–particle interface to the diffusive mass transfer rate inside the macropores. For spherical particles, the external mass transfer coefficient in a stagnant fluid is given by $k_{mo} = \mathscr{D}/(d_p/2)$, where $\mathscr{D}$ is the molecular diffusivity of the condensable vapor. The Thiele number is the ratio of the adsorption rate at the pore walls to the diffusive mass transfer rate inside the macropores [22, 54, 110]. In the context of the Langmuir theory—used to describe the adsorption of vapor molecules from the macropores to the solid structure of the particle—the Thiele number is parameterized by the maximum concentration in the solid, $q_{\max}$; the particle porosity, ϵ_p (defined as the total pore volume divided by the particle volume); and the adsorption rate coefficient, k_1. For $\Phi \gg 1$ the adsorption rate is much larger than the diffusion rate, and a vapor molecule is likely to be absorbed before it can diffuse far into the macroporous structure of the particle. It is assumed that the adsorbed phase concentration in the solid is much smaller than the maximum uptake capacity and that the macropore concentration reaches a quasi-steady state instantly [43, 118]. All particles are assumed to be homogeneous macroporous structures with a finite uptake capacity [87].

2.3 Particle Injection Through a Round Nozzle

During ACI, PAC flows into the highly turbulent flue gas where it adsorbs gas-phase mercury. We simulate the flow of microscale particles through a round nozzle in an isothermal ($T = 300\,\text{K}$) flow. The Reynolds number is $Re_D = 3000$; the computational domain is $12D \times 8D \times 8D$ in the x, y, and z directions and is covered by a grid comprised of $1024 \times 640 \times 640$ points. The resolution is clustered in the neighborhood of the shear layers to ensure grid-independent results.

2.3.1 Particle Dispersion

The fluid–particle field downstream of a nozzle [used for ACI] is shown in Fig. 2.1. The image shows an instantaneous view of $d_p = 0.1\,\mu\text{m}$, $d_p = 1\,\mu\text{m}$, and $d_p = 10\,\mu\text{m}$ particles and near vortices downstream of the nozzle. The vortices form as the

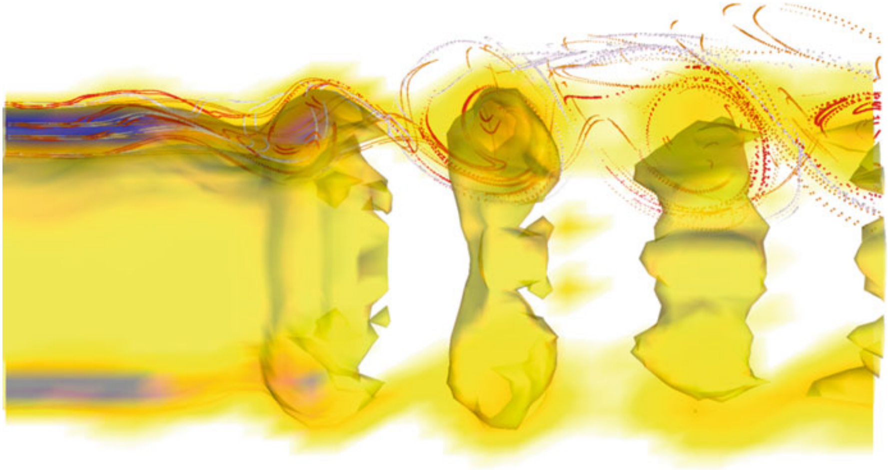

Fig. 2.1 Instantaneous micro-particle streak lines in the neighborhood of vortex rings

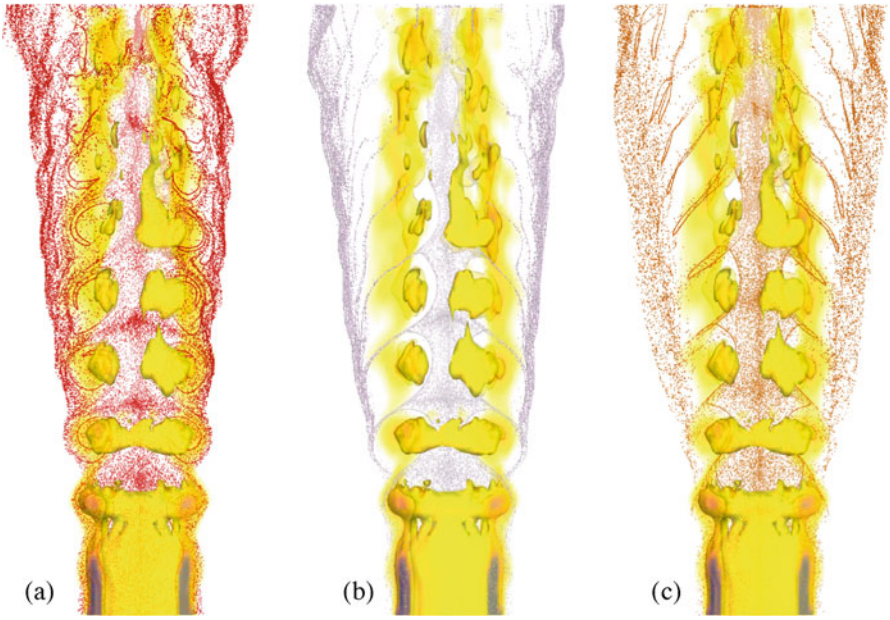

Fig. 2.2 Instantaneous snapshot of particle locations: (**a**) 0.1 µm; (**b**) 1 µm, and (**c**) 10 µm

jet transitions from a laminar flow to a turbulent one. The particle traces indicate that the particles have different trajectories. This is more clearly observed in Fig. 2.2. For clarity, and the purposes of illustration, roughly 10,000 particles are shown in each image. As the flow travels downstream, the jet entrains the background fluid, and the particles are dispersed. (In the case of ACI, the background fluid would be flue gas containing mercury vapor.) Figure 2.2a shows that the $d_p = 0.1\,\mu\text{m}$ particles are fairly well dispersed across the jet, with particles present near the centerline, in the eddies, and at the jet periphery. However the image reveals that particles are accumulating at the outer part of the flow, indicating that a large number of the smaller $0.1\,\mu\text{m}$ particles have crossed into the slower-moving background flue gas. These particles are relatively inertialess and follow the fluid. Figure 2.2b shows a similar distribution pattern for the $1\,\mu\text{m}$ particles. There are particles located in the core of the jet, and there is accumulation at the periphery. However the vortex cores are virtually devoid of the $1\,\mu\text{m}$ particles, the vortices that transported all particles in their vicinity into the slower-moving background fluid. A snapshot of the largest $10\,\mu\text{m}$ diameter particles shown in Fig. 2.2c reveals that fewer particles have made it into the background fluid. While most particles are found along the jet centerline, some are in the process of being "flung" across the vortex cores. Turbulent mixing, including large-scale mixing via eddies, can greatly increase the residence or contact time between the particles and the background condensable vapor and thus adsorption.

2.3.2 Particle Reynolds Number

The particle velocities and trajectories are a function of the drag, the Stokes number, and the slip velocity. While the Stokes number is fixed, the drag correction factor is a function of the particle Reynolds number, $Re_p = |u_i - u_{i,p}|Re_{po}$. Similarly, the mass transfer rate is given by the Sherwood number and is a function of the particle Reynolds number. Histograms of the particle Reynolds number for the 0.1, 1, and $10\,\mu\text{m}$ diameter particles are shown in Fig. 2.3a. The figure shows a unimodal distribution of particle Reynolds numbers for the $0.1\,\mu\text{m}$ diameter particles, with

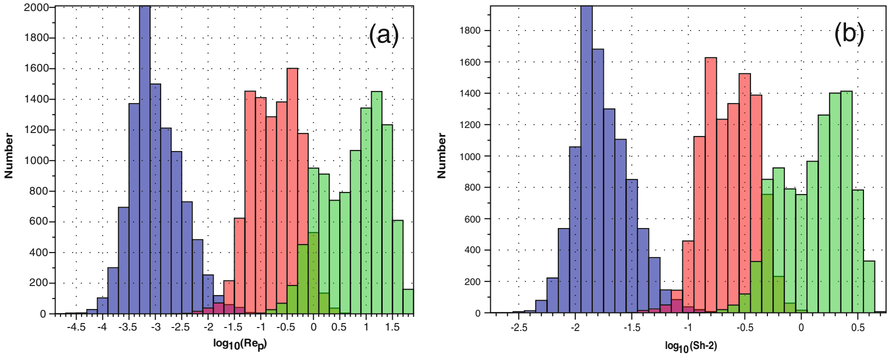

Fig. 2.3 Instantaneous distributions of (**a**) particle Reynolds number, Re_P, and (**b**) Sherwood number, Sh, with a function of particle diameter ($0.1\,\mu\text{m}$ particles in *blue*, $1\,\mu\text{m}$ particles in *red*, and $10\,\mu\text{m}$ particles in *green*)

mean values around $Re_p = 0.001$. There are three readily observed trends. First, as the particle size increases, the distribution of Re_p values moves to the right. The mean particle Reynolds number for the 1 µm and 10 µm diameter particles is roughly $Re_p = 0.25$ and $Re_p = 5$, respectively. These increasing values show that as the particles get larger, more mercury vapor is adsorbed onto their surface. The second trend is that as the particles get larger, the distribution moves from a unimodal (for the 0.1 µm particles) to bimodal (10 µm particles). (The 1 µm particles show a more broad unimodal distribution.) A small tail develops as the distribution moves to the right—roughly at $Re_p = 1$ for the 10 µm particles. This value is much lower than the peak value and suggests that these particles are moving more slowly relative to the fluid. That is, they have overcome their initial inertia and moving "with" the fluid, compared to the particles with larger particle Reynolds numbers. The third trend observed is that most particles experience lower particle Reynolds numbers. These trends are also observed in the Sherwood number. As *Sh* shifts farther right, the count decreases. This reveals that fewer particles experience the high gas-to-particle mass transfer conditions.

Obtaining a more quantitative view of the mass transfer dynamics is difficult because of the compute time. The particle residence time in the computational domain is on tens of milliseconds. As a result, the time that the particles and background gas is relatively low. Each computation of the jet flow required roughly 2×10^5 CPU-hours.

2.4 Multiphase Mixing Layer Transport

Simulations of temporal mixing layers are performed to obtain a more detailed view of the fluid–particle mixing. The configuration is such that the upper half of the mixing layer contains mercury vapor, while the lower half contains the microscale particles. As the flow develops, the two streams come into contact, and condensation occurs. A reference frame is attached to the fluid and moves with the mean velocity, as shown in Fig. 2.4. In doing so, the simulation is transformed from a spatially developing one to a temporally developing one. The flows under consideration are

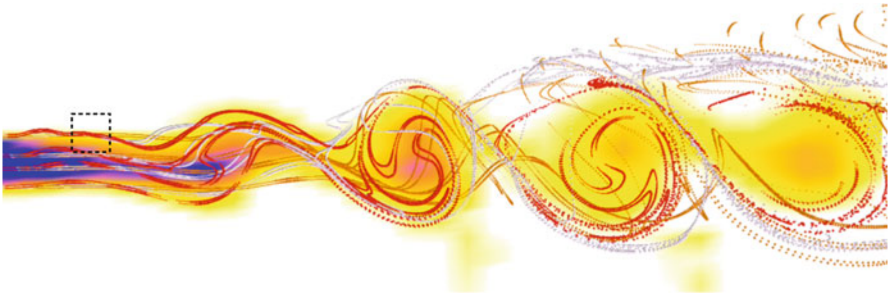

Fig. 2.4 Particle field close-up indicating area for temporal flow simulation

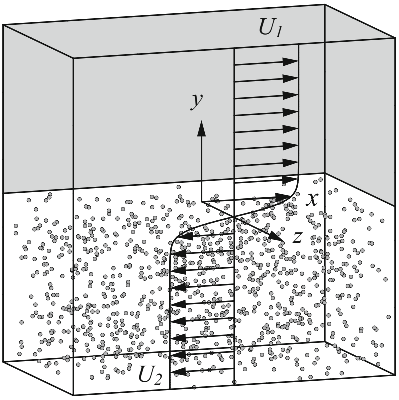

Fig. 2.5 Particle-laden temporal mixing layer flow configuration

three-dimensional incompressible mixing layers. A temporal mixing layer is formed when two parallel streams which travel in opposite direction meet [75, 96]. The streams mix and entrain fluid through large-scale coherent structures [9, 12, 85]). The spatial coordinates are $\mathbf{x} = (x, y, z)$ in streamwise, cross-stream, and spanwise directions, respectively, as shown in Fig. 2.5. The corresponding velocities are $\mathbf{u} = (u, v, w)$. Initially, the upper stream contains condensable vapor, and the lower stream contains uniformly distributed particles. As the flow evolves in time, vapor and particles are mixed, and mass is transferred from the gas phase to the particle phase through condensation.

2.4.1 Physical Parameters

The Reynolds number for all flows is $Re_L = 450$ and is based on the initial 99%-boundary layer thickness, $L = \delta$, and one half of the velocity difference across the two streams $U_o = 0.5 \times (U_1 - U_2)$. The Schmidt number for the condensable vapor is $Sc = 1.1$. To elucidate the effect of the governing parameters, six simulations are performed for different values of the reference particle Reynolds number, Re_{po}; the parameter A; the particle Stokes number, St_k; the reference mass Biot number, Bi_{mo}; and the Thiele number, Φ, as listed in Table 2.1. Case 1a is the base case, representing typical operating conditions of an ESP where carbon particles with diameter $d_p = 10\,\mu\text{m}$ are used to remove mercury vapor from flue gas at atmospheric pressure and a temperature of $T = 500\,\text{K}$ [17, 18]. Activated carbon particles of type Darco® G60 are considered, which have a porosity of $\epsilon_p = 0.65$ and a bulk density of $\rho_p = 450\,\text{kg/m}^3$ [45, 46, 97–99]. Starting from case 1a, the governing parameters are changed separately. In case 2, the parameter A is set to $A = 10^{-3}$; the reference particle Reynolds number is $Re_{po} = 25.3$, since A and Re_{po} are not independent and the Reynolds and Schmidt number remain unchanged

Table 2.1 Simulation parameters for cases 1a–d, case 2, and case 3

Case	1a	1b	1c	1d	2	3
Particle Reynolds number, Re_{po}	1.32	1.32	1.32	1.32	25.3	1.32
Parameter A ($\times 10^5$)	5.2	5.2	5.2	5.2	100	5.2
Stokes number, St_k	0.17	0.17	0.17	0.17	0.17	10.0
Mass Biot number, Bi_{mo}	0	10	181	181	0	0
Thiele number, Φ	∞	10	10	0.2	∞	∞

in all simulations. Case 3 differs from case 1a in that the particle Stokes number is increased from $St_k = 0.17$ to $St_k = 10$. Mass transfer resistances associated with intra-particle diffusion and sorption kinetics are neglected altogether in cases 1a, 2, and 3. That is, particles are assumed to be perfect sinks, which mathematically corresponds to $Bi_{mo} \rightarrow 0$ and/or $\Phi \rightarrow \infty$. Cases 1b, 1c, and 1d are derived from case 1a. The perfect sink assumption, however, is dropped and (2.9) is used to compute the non-zero surface concentration. In case 1b, the mass Biot number and the Thiele number are $Bi_{mo} = 10$ and $\Phi = 10$, respectively. In case 1c the mass Biot number is increased to $Bi_{mo} = 181$, and the Thiele number is held constant at $\Phi = 10$. Finally, in case 1d, the Thiele number is decreased to $\Phi = 0.2$, and the mass Biot number is held constant at $Bi_{mo} = 181$. The latter case represents sorption properties of Darco® G60 carbon blacks at a temperature of $T = 500$ K.

2.4.2 Numerical Specifications

The governing fluid transport equations are solved using a MacCormack-based finite difference scheme [14, 67]. The accuracy of the scheme is second order in time and fourth order in space. A first order accurate forward difference scheme is used to solve for the particle position, velocity, and mass as a function of time. The number of particles in the domain is $N_p = 50{,}000$. Since the fluid–particle transport equations are solved in a mixed Eulerian/Lagrangian framework, respectively, an interpolation algorithm is required to obtain the fluid transport variables at the particle locations. To this end, a linear interpolation scheme is used. Computations are performed on a domain of $2\pi \times 2\pi \times 1.2\pi$ in x, y, and z directions, respectively. Periodic boundary conditions are used in x and z directions, while free-stream boundary conditions are applied in y direction at the upper and lower boundaries of the domain, that is, the y-velocity component and the first derivative of all other transport variables vanish. The periodic conditions imply that fluid and particles, exiting through the left, right, rear, or front boundary, are reintroduced through the opposite boundary. The computational grid is comprised of $512 \times 512 \times 320$ evenly spaced grid points [19, 44].

2.4.3 Fluid Field and Particle Dispersion

The initial conditions are chosen such that four vortices are formed in streamwise direction. After the onset of the simulation, at time $t = 3$, a first vortex pairing is observed. Subsequently, the flow breaks up into smaller scales and grows in the nonperiodic direction, y, perpendicular to the mixing layer. Figure 2.6 shows an iso-surface of vorticity magnitude, $|\omega| = 1$, along with particle locations at four different times, obtained in case 1a. For purposes of illustration, only a subset of the domain is shown. Figure 2.6a reveals that, at time $t = 5$, particles accumulate in the periphery of the vortex and are thus entrained into the upper stream by means of large-scale mixing. Figure 2.6b and c illustrate the formation of streamwise vortical structures and continuous entrainment of particles into the upper stream at time $t = 10$ and $t = 20$, respectively. The simulation is stopped at time $t = 30$ before the size of the eddies becomes too large to be contained within the flow domain.

The effect of the unsteady flow field on particles with different Stokes numbers is illustrated in Fig. 2.7. Instantaneous vorticity contours are shown in the xy-plane, at $z = 0$, along with particle locations at time $t = 5$ and $t = 30$, obtained in case 1a and case 3. The vorticity fields are identical in both cases, as the particles do not affect the flow field [76, 77]. The particle dispersion patterns, however, are different. The particles in the $St_k = 0.17$ flow (case 1a) follow the fluid motion more closely than those in the $St_k = 10$ flow (case 3). Figure 2.7a reveals that, at time $t = 5$, particles in the $St_k = 0.17$ flow are engulfed in the growing vortices. By contrast, Fig. 2.7b shows that, at the same time, only few particles with $St_k = 10$ are carried along by the eddies. At time $t = 30$, a preferential concentration of $St_k = 0.17$ particles is observed, aligned with vorticity contours. Particles with Stokes numbers much larger than unity do not exhibit this behavior [42, 107].

Figure 2.8 provides insight into particle dispersion parallel to the mixing layer or the orientation of the particles with streamwise flow structures. Instantaneous vorticity contours and particle positions are shown in the xz-plane, at $y/\pi = -0.2$, obtained in case 1a and case 3 at time $t = 30$. Figure 2.8a reveals that particles with $St_k = 0.17$ preferentially collect in regions of low vorticity, as was pointed out earlier by other researchers [55, 107]. Figure 2.8b shows that particles with $St_k = 10$ (case 3) exhibit distinct streamwise patterns, although the alignment with low vorticity regions is not as pronounced as in the $St_k = 0.17$ flow.

A more quantitative measure of particle dispersion across the mixing layer is the probability density function (pdf) of the particles migrating into the upper, condensable vapor-containing, stream. The pdfs of the particle y-location, $f(y_p)$, for all cases are shown in Fig. 2.9 at four different times. The dot-dashed line indicates the initial condition, with all particles being uniformly distributed in the lower stream, $-1 \leq y_p/\pi \leq 0$, where $f(y_p)$ is unity. The pdfs obtained in case 1a and case 2 are almost identical, implying that the nondimensional particle relaxation time, St_k/f_p, is approximately equal in both cases, even though the reference particle Reynolds number, Re_{po}, differs. Figure 2.8a shows that, at time $t = 5$, only a small fraction (0.6%) of the particles in the $St_k = 10$ flow (case 3) have entered the

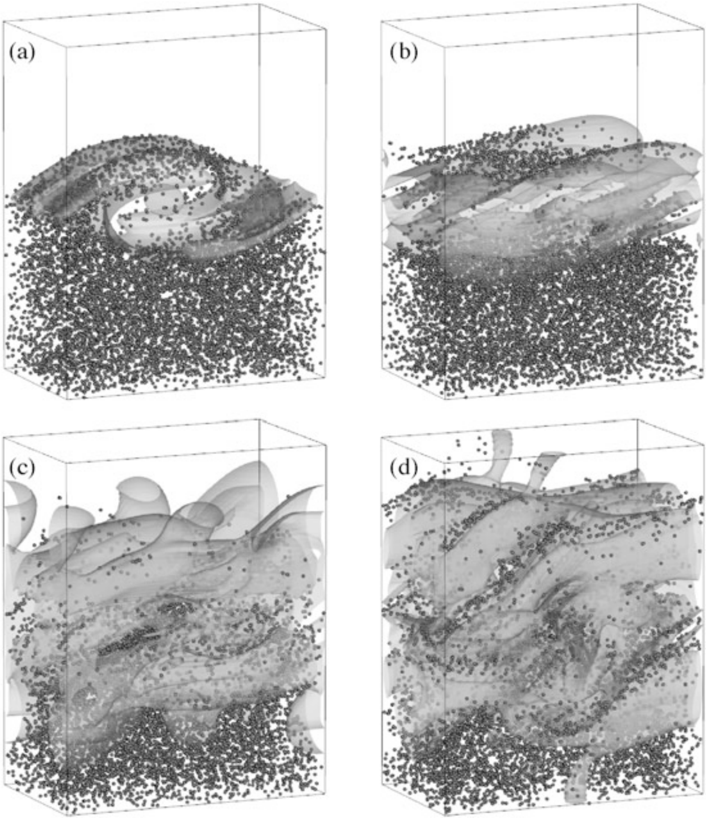

Fig. 2.6 Instantaneous vorticity magnitude iso-surface, $|\omega| = 1$, and particle locations, obtained in case 1a at time: (**a**) $t = 5$; (**b**) $t = 10$; (**c**) $t = 20$; (**d**) $t = 30$. The domain range shown is $0 \leq x/\pi \leq 1$, $-2 \leq y \leq 2$, and $0 \leq z/\pi \leq 0.6$

upper stream. At the same time, an order of magnitude more particles (6%) in the $St_k = 0.17$ flows (cases 1a and 2) are entrained by the upper stream. At time $t = 10$, Fig. 2.9b shows an accumulation of particles in the $St_k = 0.17$ flows at the periphery of the eddies, near $y_p/\pi = \pm 0.2$. Figure 2.9c shows that the fraction of particles in the upper stream of the $St_k = 0.17$ flow remains nearly constant and does not exceed 6% until time $t = 20$. At time $t = 30$, Fig. 2.9d shows that the number of particles entrained by the upper stream is approximately twice as much in cases 1a and 2 than in case 3.

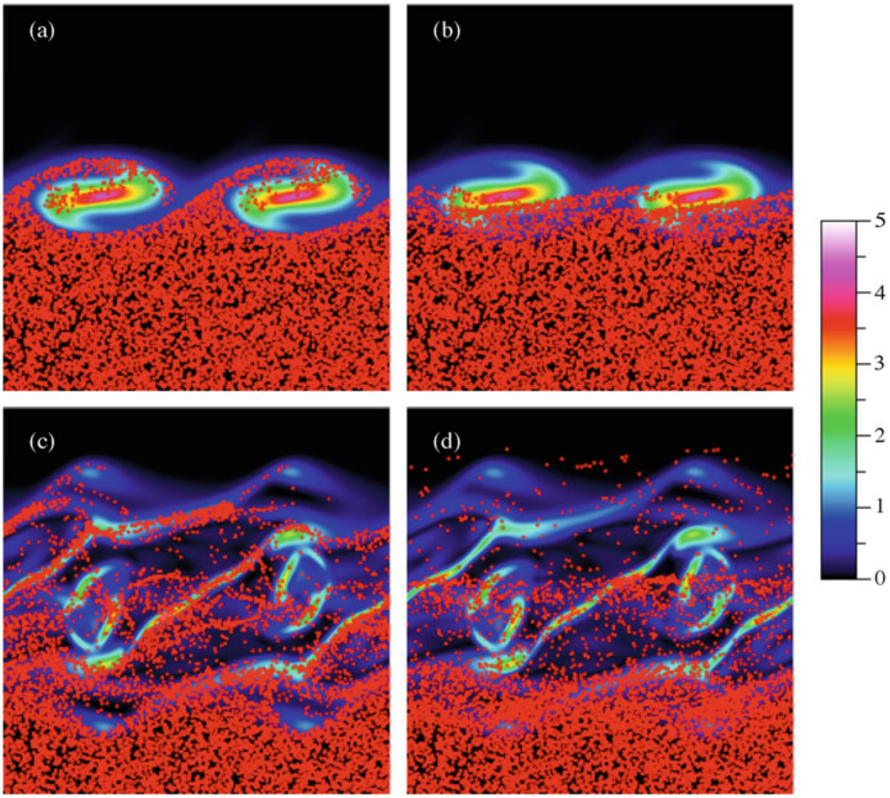

Fig. 2.7 Instantaneous vorticity magnitude contours and particle locations in the *xy*-plane at $z = 0$: (**a**) case 1a, time $t = 5$; (**b**) case 3, $t = 5$; (**c**) case 1a, $t = 30$; (**d**) case 3, $t = 30$

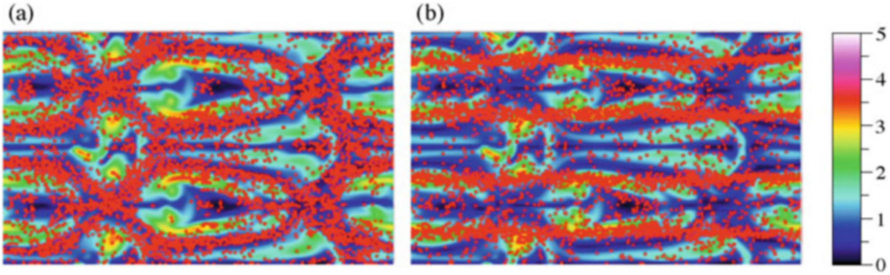

Fig. 2.8 Instantaneous vorticity magnitude contours and particle locations in the *xz*-plane at $y/\pi = -0.2$ and time $t = 30$: (**a**) case 1a; (**b**) case 3

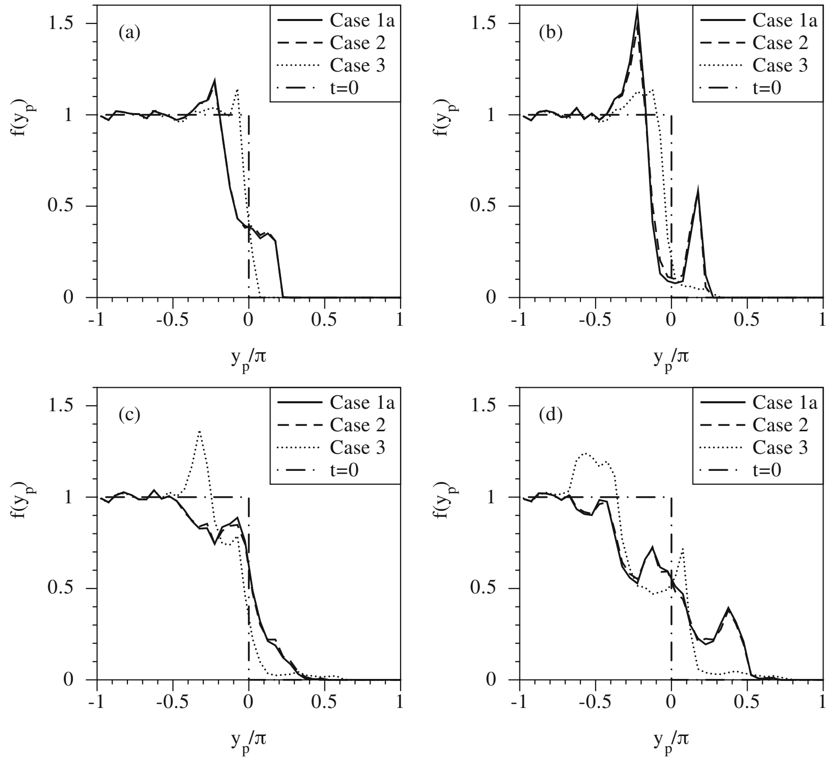

Fig. 2.9 Instantaneous pdfs of the particle y-location, $f(y_p)$, at time: (**a**) $t = 5$; (**b**) $t = 10$; (**c**) $t = 20$; (**d**) $t = 30$

2.4.4 Mass Transfer

The Sherwood number, Sh, is a governing parameter for gas–particle mass transfer. It accounts for the diffusive flux as well as the increased mass transfer due to a gas–particle slip velocity, Δu_i. The Sherwood number is modeled as a function of the particle Reynolds number, Re_p, which in turn depends on Δu_i (2.8). Research has shown that the particle slip velocity grows with increasing Stokes numbers [95]. The lower the Stokes number, the more closely particles follow streamlines and the lower the gas–particle slip velocity becomes. The gas–particle slip velocity vanishes in the limiting case of $St_k \rightarrow 0$. Hence, particles in the $St_k = 10$ flow (case 3) exhibit a higher gas–particle slip velocity than those in the $St_k = 0.17$ flows (case 1a and case 2). The mean gas–particle slip velocities for particles with $St_k = 0.17$ are $\overline{|\Delta u_i|} = 0.014$ and $\overline{|\Delta u_i|} = 0.013$ in case 1a and case 2, respectively. (An overline denotes a quantity averaged over all particles at time $t = 30$.) The difference can be attributed to a different reference particle Reynolds number, which has an influence on the particle motion through the drag correction

Table 2.2 Mean quantities, surface concentration, and overall mass removal for cases 1a–d, case 2, and case 3

Case	1a	1b	1c	1d	2	3
Slip velocity, $\overline{\|\Delta u_i\|}$	0.0145	0.0145	0.0145	0.0145	0.0134	0.1431
Reynolds number, $\overline{Re_p}$	0.0191	0.0191	0.0191	0.0191	0.3405	0.1894
Sherwood number, $\overline{Sh}$	2.0663	2.0663	2.0663	2.0663	2.2813	2.2014
Surface concentration, $c_s(Bi_{mo}, \Phi)$	0	0.5263	0.9527	0.9999	0	0
Mass removal, $\Theta(t = 30)$	7.8%	4.3%	0.5%	<0.1%	23.6%	8.5%

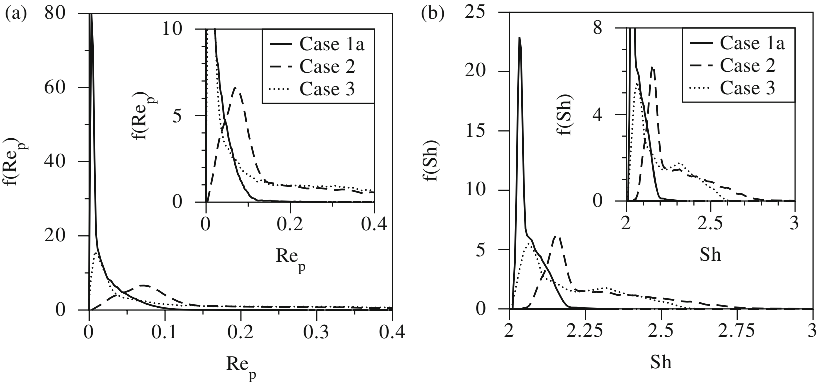

Fig. 2.10 Instantaneous pdfs of (**a**) the particle Reynolds number, $f(Re_p)$, and (**b**) the Sherwood number, $f(Sh)$, at time $t = 30$

factor, f_p. For particles with $St_k = 10$ (case 3), the mean gas–particle slip velocity is $\overline{|\Delta u_i|} = 0.1431$, which is one order of magnitude larger than the $St_k = 0.17$ cases. Mean quantities are listed in Table 2.2.

Figure 2.10a shows pdfs of the particle Reynolds number, $f(Re_p)$, which is related to the gas–particle slip velocity through $Re_p = |\Delta u_i| Re_{po}$. As a result of the augmented particle slip velocity in case 3, the mean particle Reynolds number is larger in case 3 than in case 1a. The largest particle Reynolds numbers, Re_p, are observed in case 2, owing to the large reference particle Reynolds number, $Re_{po} = 25.3$. However, the particle Reynolds numbers are less than unity even in case 2, which results in a drag correction of less than 15% (i.e., $f_p - 1 < 0.15$) and explains why there is no significant difference in terms of particle dispersion between case 1a and case 2. It is therefore adequate to use Stokes law to describe particle motion. The mean particle Reynolds numbers are $\overline{Re_p} = 0.02$, $\overline{Re_p} = 0.34$, and $\overline{Re_p} = 0.19$ in case 1a, case 2, and case 3, respectively. Finally, the pdfs of the Sherwood number, $f(Sh)$, are presented in Fig. 2.10b. The correlation between the Sherwood number and the particle Reynolds number is given by Eq. (2.8). Consequently, the mean Sherwood number is largest in case 2, intermediate in case 3, and smallest in case 1a. The pdfs $f(Sh)$ all have a distinctive left-skewed shape with a minimum value of $Sh = 2$, which corresponds to mass transfer in

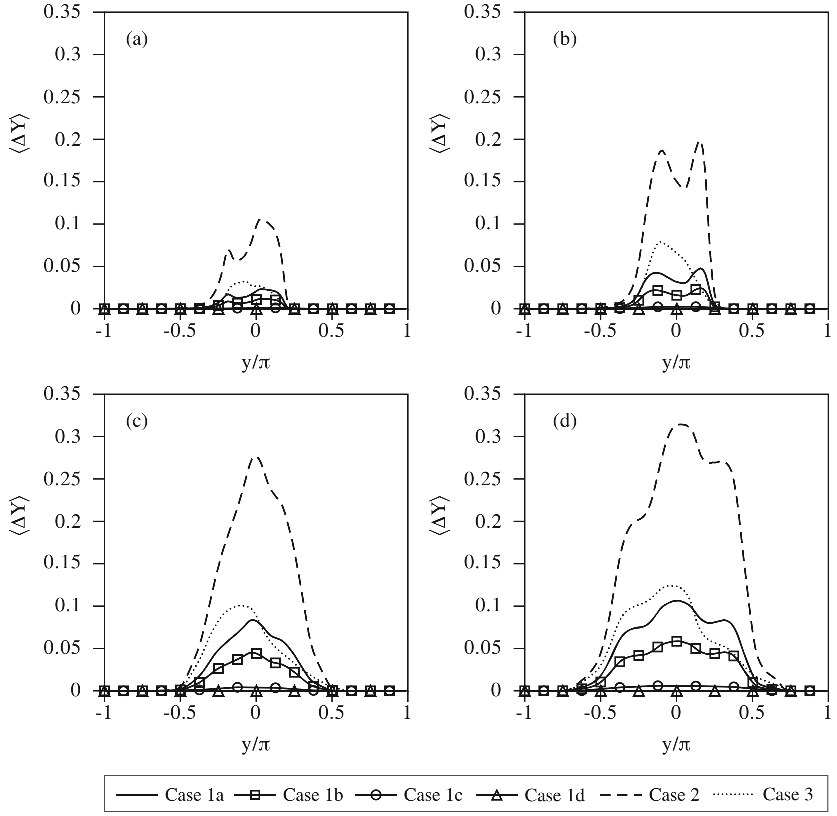

Fig. 2.11 Cross-stream profiles of the condensable vapor mass fraction removed from the fluid, $\langle \Delta Y \rangle$ at time: (**a**) $t = 5$; (**b**) $t = 10$; (**c**) $t = 20$; (**d**) $t = 30$

a stagnant fluid, purely due to diffusion. Convective effects at the particle surface, resulting from a non-zero particle slip velocity, become manifest in $Sh > 2$ values. Hence, on average, convective effects act to increase mass transfer by 3% in case 1a ($\overline{Sh}/2 = 1.033$), 14% in case 2 ($\overline{Sh}/2 = 1.14$), and 10% in case 3 ($\overline{Sh}/2 = 1.10$).

Cross-stream profiles of the vapor mass fraction removed by condensation, $\langle \Delta Y \rangle$, are presented in Fig. 2.11 for all cases at four different times. (The brackets $\langle \cdot \rangle$ denote a quantity averaged in x- and z-direction.) The ordinate spans across the height of the mixing layer $-1 \leq y/\pi \leq 1$. Profiles are obtained by comparing averaged species profiles, $\langle Y \rangle$, against a simulation without mass transfer. Initially, all particles are located in the region $y < 0$, and vapor is contained in the region $y > 0$ only. Figure 2.11a reveals that, at time $t = 5$, vapor is removed in the range $-0.5 \leq y/\pi \leq 0.25$ where particles mix with vapor. This range broadens with time, as particle dispersion increases and more vapor is entrained into the lower stream. It was shown in Fig. 2.9 that only few particles with $St_k = 10$ enter the upper stream. Consequently, mass is predominantly removed from the lower stream

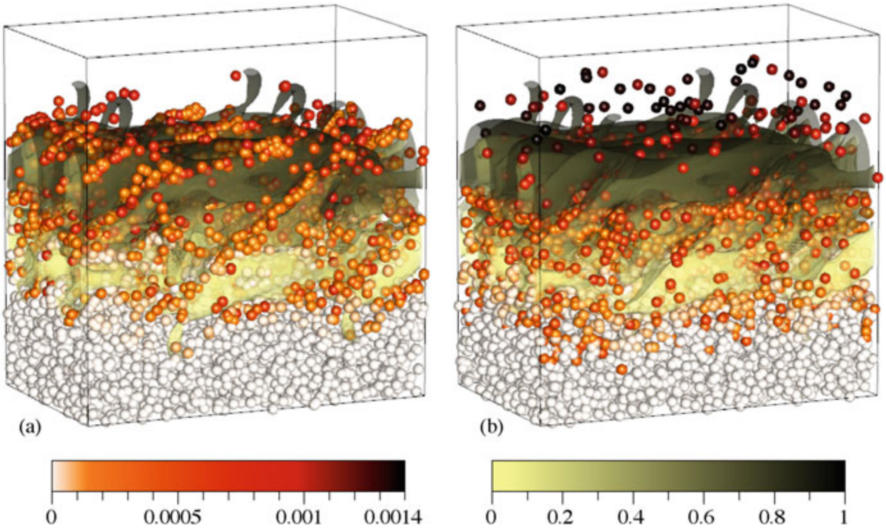

Fig. 2.12 Instantaneous vorticity iso-surface (magnitude = 1) and particle locations at time $t = 30$ in (**a**) case 1a and (**b**) case 3. Only 10,000 particles are shown for clarity. The iso-surface is colored based on the local vapor mass fraction. The *color* of the particles represents the mass of vapor accumulated on the particle

in case 3, which can be concluded from a left-skewed shape of the profile in that case. In all other cases, where particle dispersion is increased, more mass is removed from the upper stream. The highest mass removal is achieved in case 2, where the parameter A has a value of $A = 10^{-3}$. The lowest mass removal is observed in case 1d, where the surface concentration is $c_s = 0.9999$ owing to a large mass Biot number ($Bi_{mo} = 181$) and a small Thiele number ($\Phi = 0.2$), cf. Table 2.2.

A qualitative view of the particle transport and gas adsorption dynamics is shown in Fig. 2.12. The image shows the particle locations, mass captured by the particles, vapor mass fraction, and an iso-surface of vorticity. The results for case 1a are shown in Fig. 2.12a, and the results for case 3 are shown in Fig. 2.12b. The contortions of iso-surface ($|\omega| = 1.5$) reflect that the flow has transitioned to turbulence. The images reveal that the particles in case 3 have captured more vapor than those in case 1a. However the differences appear to be significant only for those particles that have migrated into the upper part of the domain. The increased Stokes number and particle Reynolds number (due to the greater slip velocity, Δu_i) increase the Sherwood number vis a vis Eq. (2.8).

The fraction of vapor removed from the fluid by condensation is given by

$$\Theta(t) = 1 - \frac{\int\int\int Y(x,y,z,t)dxdydz}{\int\int\int Y(x,y,z,t=0)dxdydz}, \tag{2.10}$$

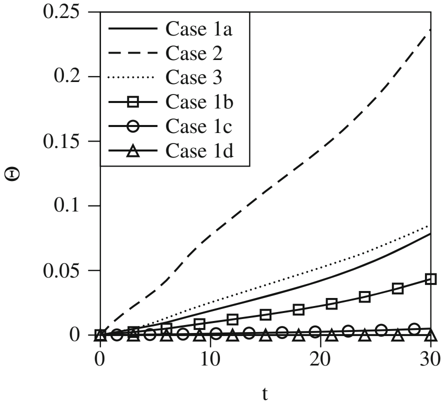

Fig. 2.13 Temporal evolution of the fraction of vapor, Θ, removed from the fluid

where $Y(x, y, z, t = 0)$ is the vapor mass fraction at time $t = 0$. The temporal evolution of Θ is presented in Fig. 2.13. The highest vapor removal is observed in case 2. This can be attributed to two separate effects: firstly, to an increased mass transfer rate due to convection (high $\overline{Sh}$) and, secondly, to the large value of the parameter A. The amount of vapor removed at time $t = 30$ is listed in Table 2.2 for all cases. Particles with $St_k = 10$ (case 3) remove more vapor than particles with $St_k = 0.17$ (case 1a) as a result of an increased gas–particle slip velocity. The lowest removal is achieved in cases 1b, 1c, and 1d, where the perfect sink assumption is not used and hence the surface concentration approaches a value of $c_s = 1$. The results presented in Figs. 2.11 and 2.13 emphasize that mass removal is greatly overpredicted if the perfect sink assumption is used.

2.5 Summary and Conclusions

In this chapter, we considered gas-to-particle mass transfer in turbulent flows. We performed DNS of round jets and temporal mixing layers. The round jet simulations mimic the nozzle region in ACI while the temporal mixing layer allows us to perform high-resolution simulations and capture the fluid–particle interactions in more depth. All flows consisted of a particle-laden stream, initially containing uniformly distributed particles, mixing with a particle-free stream containing condensable vapor. The fluid field was obtained by solving the incompressible Navier–Stokes equations in a Eulerian frame of reference, while a Lagrangian formulation was used to describe particle motion. The fluid and particle fields were coupled through gas–particle mass transfer of condensable vapor.

The jet simulations reveal the dynamics of the 0.1, 1, and 10 μm diameter porous particles. We quantified the effect of particle size on particle Reynolds numbers—the nondimensional parameter determining drag/dispersion and mass transfer. While the smaller particles are more readily dispersed across the span of the flow, and in the vortices, it is the larger particles that exhibit the greatest slip or relative velocities. This increased slip velocity results in increased condensation mass transfer.

The temporal mixing layer simulations revealed that the overall mass removal rate increases when the parameter A is increased. An increase in A corresponds to an increase in the diffusive mass transfer to the particle surface. Additionally, it was shown that mass removal is overpredicted if the perfect sink assumption is used. From an engineering point of view, mass transfer can be increased in several ways: (1) increasing the gas–particle slip velocity, (2) increasing the specific particle surface area, or (3) using highly reactant sorbent particles (large Thiele numbers). The computational model presented in this work can be used to predict condensation mass transfer under turbulent flow conditions. Unlike previous studies, it accounts for increased mass transfer due to convective effects in the boundary layer of the particles.

Unfortunately the use of DNS to simulate turbulent flows in industrial scale ductwork is yet out of reach from a computational expense point of view. Alternative modeling strategies are needed for use in the industrial engineering context. The techniques need to be capable of describing/capturing particle motion and gas-to-particle mass transfer in a sufficiently accurate manner.

Chapter 3
LES of Particle Dispersion and Gas-to-Particle Mass Transfer in Turbulent Shear Flows

Abstract LES of condensation gas-to-particle mass transfer in turbulent incompressible mixing layers are performed. The flows are comprised of a particle-free condensable vapor mixing with micron-size porous particles. Simulations are performed at a single Reynolds number while varying the particle Stokes number, the mass transfer and convective time scales, and the vapor concentration at the particle surface. DNS has shown to be quite useful in capturing the fluid–particle interactions though at a high compute time. The goal of this work is to use LES to obtain a high level of fidelity to the DNS but with significantly reduced computational requirements.

3.1 Introduction

The computational intensity of DNS renders it impractical for use in engineering computations. When turnaround times of hours or days are needed, the methodologies of choice are RANS and LES. LES is regarded as lying somewhere between the DNS and RANS [28, 65, 84, 101, 113]. LES has the advantage of DNS in that it captures (or *tries* to capture) the unsteady evolution of the large-scale flow features, and it has the advantage of RANS in that it allows for inclusion of realistic flow and chemistry parameters. Of course, the closure problem as encountered in RANS is also present in LES. However, since only the effects of the small scales are modeled in LES, the closure uncertainties at such scales are less damaging than those in RANS in which modeling is applied at all scales.

Large eddy simulation (LES) facilitates the solution of the spatially (and/or temporally) filtered governing equations [2, 35]. The transport variables are decomposed into their resolved and unresolved or subgrid-scale (SGS) components and the Navier–Stokes equations filtered. The nonlinear interactions between the large and small scales are prescribed by the large eddies only, and the mathematical form is provided by SGS closures [80, 90, 114]. Improvements in modeling the SGS stresses have been widespread since the original Smagorinsky closure [27, 50, 59, 63, 80, 84, 90, 105, 113]. The dynamic approach proposed by Germano et al. [36] allows the evaluation of the model "constant" as a function of space and time. This approach accommodates the backscatter of energy not permitted when

S.C. Garrick, M. Bühlmann, *Modeling of Gas-to-Particle Mass Transfer in Turbulent Flows*, SpringerBriefs in Applied Sciences and Technology,
DOI 10.1007/978-3-319-59584-9_3

using a fixed value and has been shown to be an improvement [33, 35, 36, 114]. The closures which are not eddy viscosity-based closures have shown promise for LES for turbulent flows. Scale-similarity approaches which use both single- [7] and multiple-scale filters [71] predict SGS stress tensors which are very close to their exact counterparts. Advanced methodologies such as the joint velocity filtered density function have shown to be quite successful, though they are a bit more computationally expensive than zero-equation closures [37].

We utilize LES to capture the condensation of vapor onto micron-size particles in turbulent mixing layers. The motivation is twofold: to obtain the dynamics described in Chap. 2 and to significantly reduce the compute time.

3.2 Formulation

3.2.1 Fluid Field

The flows under consideration are described by the incompressible Navier–Stokes equations, as described in Chap. 2 are reproduced here for clarity. The conservation of mass, momentum, and species in dimensional form are:

$$\frac{\partial u_j}{\partial x_j} = 0, \tag{3.1}$$

$$\frac{\partial u_i}{\partial t} + \frac{\partial u_i u_j}{\partial x_j} = -\frac{1}{\rho}\frac{\partial p}{\partial x_i} + \frac{\partial^2 u_i}{\partial x_j \partial x_j}, \tag{3.2}$$

$$\frac{\partial Y_i}{\partial t} + \frac{\partial Y_i u_j}{\partial x_j} = \Gamma \frac{\partial^2 Y_i}{\partial x_j \partial x_j} - \omega_{Y_i} \tag{3.3}$$

where the fluid density is constant and Γ is the species mass diffusivity. In LES, removal of the “small scales” or filtering is accomplished by passing the flow variables through a convolution filter:

$$\langle g(\mathbf{x}, t)\rangle_L = \int_{-\infty}^{\infty} h_s(\mathbf{x} - \mathbf{x}')g(\mathbf{x}', t), d\mathbf{x}' \tag{3.4}$$

where $g(\mathbf{x}, t)$ is the variable being filtered with an isotropic, nonnegative definite, spatial filter, and $\langle g(\mathbf{x}, t)\rangle_L$ is the variable with the high wave number content removed [79].

The large-scale component, or the “mean,” is associated with the width of the filter $\hat{\Delta}$. The ideal value of the filter width is the one lying outside of the energy-containing range of the spectrum [2]. Applying the filter to Eqs. (3.1)–(3.3) yields:

$$\frac{\partial \langle u_j\rangle_L}{\partial x_j} = 0, \tag{3.5}$$

$$\frac{\partial\langle u_i\rangle_L}{\partial t}+\frac{\partial\langle u_i\rangle_L\langle u_j\rangle_L}{\partial x_j}=-\frac{\partial\langle p\rangle_L}{\partial x_i}+\nu\frac{\partial^2\langle u_i\rangle_L}{\partial x_j\partial x_j}-\frac{\partial\tau_{ij}}{\partial x_j}, \tag{3.6}$$

$$\frac{\partial\langle Y_i\rangle_L}{\partial t}+\frac{\partial\langle u_j\rangle_L\langle Y_i\rangle_L}{\partial x_j}=\Gamma\frac{\partial^2\langle Y_i\rangle_L}{\partial x_j\partial x_j}-\frac{\partial\theta_j}{\partial x_j}+\langle\omega_Y\rangle_L, \tag{3.7}$$

where τ_{ij} is the SGS stress representing the unresolved fluid interactions,

$$\tau_{ij}=\langle u_iu_j\rangle_L-\langle u_i\rangle_L\langle u_j\rangle_L, \tag{3.8}$$

and θ_j is the SGS fluid-scalar flux representing the unresolved fluid–chemical interactions:

$$\theta_j=\langle u_jY_i\rangle_L-\langle u_j\rangle_L\langle Y_i\rangle_L. \tag{3.9}$$

3.2.2 Particle Field

The evolution of the particle field is prescribed in Sect. 3.2.2 with the exception that the mean quantities replace their exact counterparts. For example, in describing the particle trajectories, the mean velocity $\langle u_i\rangle$ replaces u_i in Eq. (3.10) to become

$$\frac{dx_{i,p}}{dt}=\langle u_{i,p}\rangle_L,\qquad \frac{du_{i,p}}{dt}=\frac{f_p}{St_k}\left(\langle u_i\rangle_L-\langle u_{i,p}\rangle_L\right) \tag{3.10}$$

where $\langle u_{i,p}\rangle_L$ is the mean particle velocity in the x_i direction. The drag correction factor, f_p, is obtained using the filtered velocities in Eq. (2.6). Similarly the mean mass fraction, $\langle Y_i\rangle_L$, replaces the exact mass fraction, Y_i, in the governing equations describing mass transfer. In doing so, we neglect the SGS fluid–particle interactions.

3.2.3 Modeling of the SGS Stress

We consider four SGS stress closures. Three are based on the eddy viscosity concept, and the fourth is a scale-similarity model. The eddy viscosity closures assume a direct proportionality between the SGS stress and the filtered rate of strain tensor [2]. Eddy viscosity-based closures assume that the SGS stress tensor is given by

$$\tau_{ij}-\frac{1}{3}\delta_{ij}\tau_{kk}=-2\nu_t\langle S_{ij}\rangle_L=-\nu_t\left(\frac{\partial\langle u_i\rangle_L}{\partial x_j}+\frac{\partial\langle u_j\rangle_L}{\partial x_i}\right). \tag{3.11}$$

The specification of the SGS viscosity varies from closure to closure.

The Smagorinsky eddy viscosity (SEV) closure [105] parameterizes the SGS viscosity with filter width $\hat{\Delta}$ and the magnitude of the mean rate of strain tensor, $|\langle S\rangle_L|$. The SGS viscosity is given by

$$\nu_t = C\hat{\Delta}^2|\langle S\rangle_L|, \tag{3.12}$$

where the magnitude of the rate of strain is $|\langle S\rangle_L| = \sqrt{2\langle S_{ij}\rangle_L\langle S_{ij}\rangle_L}$. The constant C needs to be specified a priori.

The dynamic eddy viscosity (DEV) closure modifies the Smagorinsky model by locally computing the model coefficient [35, 36]. To do this, filtering is performed at an additional level. A test filter of width $\overline{\Delta}$ is used to define a test-filtered stress given by $T_{ij} = \overline{\langle u_i u_j\rangle}_L - \overline{\langle u_i\rangle}_L\overline{\langle u_j\rangle}_L$. The model constant is evaluated by assuming the same functional form for both the SGS stress and the test-filtered stress in conjunction with a least square minimization technique [60]:

$$C_D = \frac{1}{2}\frac{L_{ij}\, M_{ij}}{M_{kl}\, M_{kl}}, \tag{3.13}$$

where L_{ij} is computed using the Germano identity [35]

$$L_{ij} = T_{ij} - \overline{\tau}_{ij} = \overline{\langle u_i\rangle_L\langle u_j\rangle}_L - \overline{\langle u_i\rangle}_L\overline{\langle u_j\rangle}_L, \tag{3.14}$$

and M_{kl} is given by

$$M_{kl} = \overline{\Delta}^2\, |\overline{\langle S\rangle_L}|\, \overline{\langle S_{kl}\rangle_L} - \hat{\Delta}^2\, \overline{|\langle S\rangle_L|\langle S_{kl}\rangle_L}. \tag{3.15}$$

This approach is advantageous in the physical sense because it allows for the backscatter of energy while being simple to implement due to the fact that the "constant" does not need to be specified a priori.

The modified kinetic energy viscosity (MKEV) closure is similar to that of Bardina et al. [7] which relates the turbulent kinetic energy to the evaluation of the eddy viscosity. The model defines the eddy viscosity, ν_t, based on the kinetic energy of the mean velocity field. This mean kinetic energy is obtained through the use of an additional filter operation at width $\overline{\Delta}$ [19, 34, 44]. The eddy viscosity is given by

$$\nu_t = C_k\overline{\Delta}\sqrt{\left|\langle u_i^*\rangle_L\langle u_i^*\rangle_L - \overline{\langle u_i^*\rangle}_L\overline{\langle u_i^*\rangle}_L\right|}. \tag{3.16}$$

The scale-similarity model (SS) is based on the idea that the interactions between the large- and small-scale components of the flow field occur mainly between similar parts from each scale [6, 7, 27, 90]. The unresolved stress, τ_{ij}, is represented with a resolved stress of the same form arrived at by filtering the velocity field twice with a filter of the same width. The SGS stress is then given by

$$\tau_{ij} = C_s l_{ij} = C_s \left(\langle \langle u_i \rangle_L \langle u_j \rangle_L \rangle_L - \langle \langle u_i \rangle_L \rangle_L \langle \langle u_j \rangle_L \rangle_L \right), \tag{3.17}$$

This formulation is advantageous in that like the dynamic model, it has the ability to represent backscatter [71].

3.2.4 *Modeling of the SGS Fluid-Scalar Flux*

The modeling of fluid-scalar flux $F_j^Y = \langle u_j Y \rangle_L - \langle u_j \rangle_L \langle Y_i \rangle_L$ is performed in a manner similar to the SGS stress. With the introduction of SGS Schmidt number Sc_t, the SGS viscosity can be used to define an SGS scalar diffusivity Γ_t :

$$\Gamma_t = \frac{\nu_t}{Sc_t}. \tag{3.18}$$

The SGS diffusivity is then used in a gradient-diffusion manner to close the SGS fluid-scalar flux [26, 35, 93]:

$$\theta_j^Y = \frac{\nu_t}{Sc_t} \frac{\partial \langle Y \rangle_L}{\partial x_j}. \tag{3.19}$$

This approach is utilized in conjunction with the eddy viscosity-based closures described in Sect. 3.2.3.

The scale-similarity approach to closing the fluid-scalar flux is similar to that used in closing the SGS stress and is based on the assumptions mentioned previously. The modeled SGS fluid-scalar flux is given by

$$\theta_j^Y = C_\phi \left(\langle \langle u_j \rangle_L \langle \phi \rangle_L \rangle_L - \langle \langle u_j \rangle_L \rangle_L \langle \langle \phi \rangle_L \rangle_L \right). \tag{3.20}$$

This closure is used only in conjunction with the similarity-based SGS stress closure (Eq. (3.17)).

3.3 Evaluation of SGS Closures for LES of Gas-to-Particle Mass Transfer

The burden of reliable LES is placed on the ability to reproduce fluid fields with good accuracy. This is especially so given that we assume that fluid–particle interactions are negligible. We therefore establish the performance of our simulation methodology in reproducing physical data obtained in a flow similar to that present in ACI. Round jets have long been a case study in experimental fluid dynamics [20, 94, 117] and have also been the subject of renewed interest [8, 23, 57, 58, 106, 108]. These flows contain many of the features associated with turbulent transport: transition, self-preservation or similarity, and decay. Thus there are several regions (in time and space) in which various theories/models may be

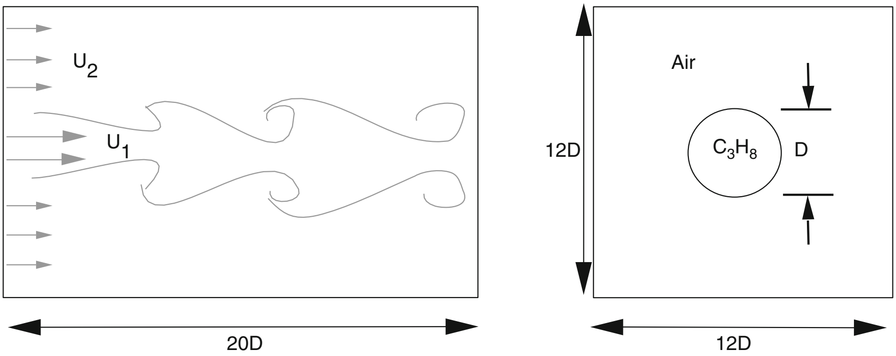

Fig. 3.1 Flow configuration for LES of round jet

tested and verified [62]. The flow consists of a fluid issuing from a round nozzle of diameter D with velocity U_1 into a co-flowing stream traveling with velocity U_2. The jet consists of propane, C_3H_8, and the co-flowing stream is air. The space coordinates are $\mathbf{x} = [x, y, z]$, where x is the streamwise direction and y and z are the cross-stream directions. A schematic of the flow configuration is shown in Fig. 3.1. The flow is chosen to approximate an experiment performed at the Sandia Turbulent Flame Facility. The experiment is on a vertical wind tunnel with an axisymmetric propane jet positioned at the upstream end of the test section. The velocity ratio is $U_1/U_2 = 7.5$, and the Reynolds number is $Re_D = U_1 D/\nu = 68{,}000$. The Mach number is $M_1 = 0.22$; hence the flow may be considered incompressible. A detailed description of the experiment and its measurements is available [100]. The scalar ϕ is used to represent the propane mass fraction, i.e., $\phi = Y_{C_3H_8}$. The Schmidt number is evaluated using a propane-into-air diffusion coefficient by a pure-species fitting procedure with a third-order polynomial resulting in a value of $Sc = 0.4$ [56]. For purposes of comparison, the experimentally obtained data are taken to be "exact."

Computations are performed on a domain of size of $20D \times 12D \times 12D$ in the streamwise and cross-stream directions, respectively. The computational grid is evenly spaced, $\Delta_x = \Delta_y = \Delta_z = \Delta$, and is comprised of $180 \times 108 \times 108$ points. The governing equations are solved using a hybrid MacCormack-based compact difference scheme [14, 67]. The numerical scheme used is based on the one-parameter family of dissipative two-four schemes developed by Carpenter [14]. The accuracy of the scheme is second order in time and fourth order in space. The exact details of the numerical schemes employed in this study are not given here, but a catalog of these schemes, and others, is readily available [14, 48]. Zero-derivative conditions are utilized at the exit plane, $x/D = 20$, and also at the cross-stream boundaries, $z/D = y/D = \pm 6$. The filter used in all simulations is the box filter which has a sharp cutoff in physical space and is given by

$$h_s(\mathbf{x}, t) = \begin{cases} \frac{1}{\hat{\Delta}} \ \text{if} |\mathbf{x} - \mathbf{x}'| \leq \frac{\hat{\Delta}}{2} \\ 0 \ \text{otherwise.} \end{cases} \tag{3.21}$$

The model constants used in the SEV and MKEV closures are $C = 0.02$ and $C_k = 0.05$, respectively. For the DEV model, the constant is allowed to be dynamically evaluated within the interval $-0.001 \leq C_D \leq 0.5$. A grid filter size of $\hat{\Delta} = \Delta$ and a test filter size of $\overline{\Delta} = 4\Delta$ are used. The SGS Schmidt number is assumed to be a constant value of $Sc_t = 1.0$. Though the values were varied, no optimization of any of the model constants and SGS Schmidt number was performed.

Both instantaneous and time-averaged data are analyzed. Time-averaged data typically employ 48,000 samples, sufficient for two sweeps of the co-flowing stream through the domain. The sampling process begins after the low-speed stream has swept through the domain once. Starting at $t^\star = 150$ all scalar values, at every grid point, are recorded. The delay in the sampling process allows the initial transients to "wash" through the domain. The sampling continues until $t^\star = 300$ is reached. Time-averaged quantities are denoted with an over-bar. These averaged data are presented as a function of radial location $r = \sqrt{y^2 + z^2}$. No averaging is performed over the azimuthal direction.

3.3.1 Fluid Field

The flow structure is depicted by the vorticity magnitude as shown in Fig. 3.2. To mimic laboratory conditions, and accelerate the transition to turbulence, perturbations of 3.5% in magnitude are added in the shear region to the cross-stream velocities v and w.

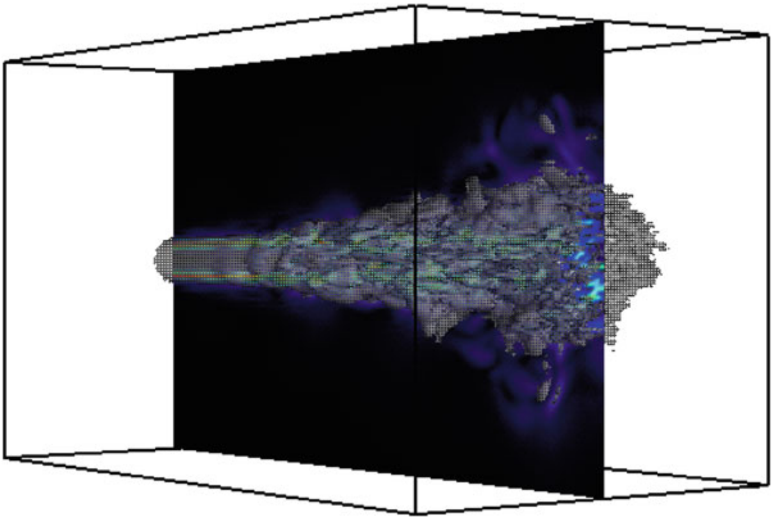

Fig. 3.2 Instantaneous vorticity magnitude, $|\omega = 2|$, iso-surface (MKEV closure)

To mimic laboratory conditions, perturbations of 3.5% in magnitude are added in the shear region to the cross-stream velocities v and w. As the flow travels in the streamwise direction, the vorticity generated at the interface of the jet and co-flowing streams evolves through bending and stretching [15, 25]. The illustrated vorticity iso-surface is roughly 33% of the peak magnitude within the computational domain, or $|\omega| = |\nabla \times \mathbf{U}| = 2.7$. Unfortunately the scale-similarity model which yielded excellent correlations in the a priori analysis did not result in a solution. Large values of the model constant C_s resulted in numerical instabilities, while small values were not dissipative enough [90]. To overcome this shortcoming, simulations were performed with a combined Smagorinsky eddy viscosity model and scale-similarity model. The SGS stress is given by

$$\tau_{ij} - \frac{1}{3}\tau_{kk}\delta_{ij} = -2\nu_t\langle S_{ij}\rangle_L + \left(l_{ij} - \frac{1}{3}l_{kk}\delta_{ij}\right) \tag{3.22}$$

where l_{ij} is given by Eq. (3.17). Results obtained by the combined model are denoted SS+SEV.

To evaluate the performance of LES in capturing the fluid velocity field, comparisons to the streamwise u-velocity at location $x/D = 15$ are shown in Fig. 3.3. The figure reveals that all models yield velocities which are within 10% of the exact values, with all closures except for the SEV yielding consistently higher values. At the jet centerline, $r = 0$, the u-velocity is 45 m/s. The MKEV closure predicts 47 m/s, while the DEV, SEV, and SS+SEV predict values between 50 and

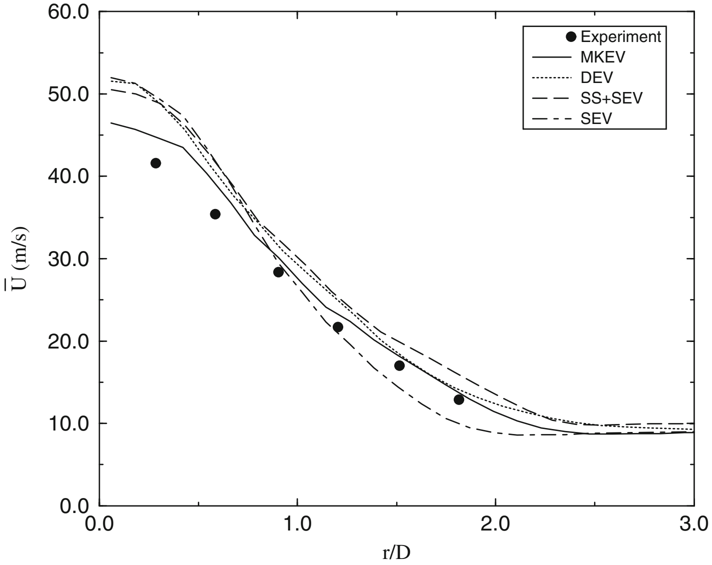

Fig. 3.3 Time-averaged radial streamwise velocity, $\overline{u}$, at $x/D = 15$

52 m/s. Further away from the centerline (increasing r), the velocities obtained by the LES remain within 10% of the exact values. Near location $r/D = 0.9$, the SEV model begins to yield velocities which are lower than the exact, with underpredictions of 10, 25, and 33% at $r/D = 1.2$, $r/D = 1.5$, and $r/D = 1.8$, respectively. In this region the MKEV and DEV closures yield values which are very close to the exact velocity. This indicates that the SEV closure predicts a reduced jet spreading rate in comparison to the other SGS closures. The jet width, δ_ω, is defined by the radial position at which the streamwise velocity is reduced by 90% of its local centerline value. Using this measure, the jet width at $x/D = 15$ is $\delta_\omega/D = 3.40$. The widths predicted by the LES are $\delta_\omega/D = 2.96$ for the SEV model, $\delta_\omega/D = 3.58$ for the MKEV and DEV models, and $\delta_\omega/D = 3.92$ for the combined SEV+SS model. The MKEV and DEV closures yield more accurate values, while the SEV closure underpredicts the jet width, and the SEV+SS closure overpredicts the jet width.

An indication of the utility of the SGS closure is the contribution of the eddy viscosity. The Reynolds number for the flow yields an equivalent viscosity of $1/Re = 1.47 \times 10^{-6}$. The SGS viscosity as provided by the MKEV closure is shown in Fig. 3.4. The image shows an instantaneous iso-surface of vorticity magnitude ($|\omega| = 0.8$) colored by the ν_t. The peak values of $\nu_t = 0.001$ show that the SGS is three orders of magnitude greater than the molecular viscosity and reflects the dissipation provided by the SGS closure.

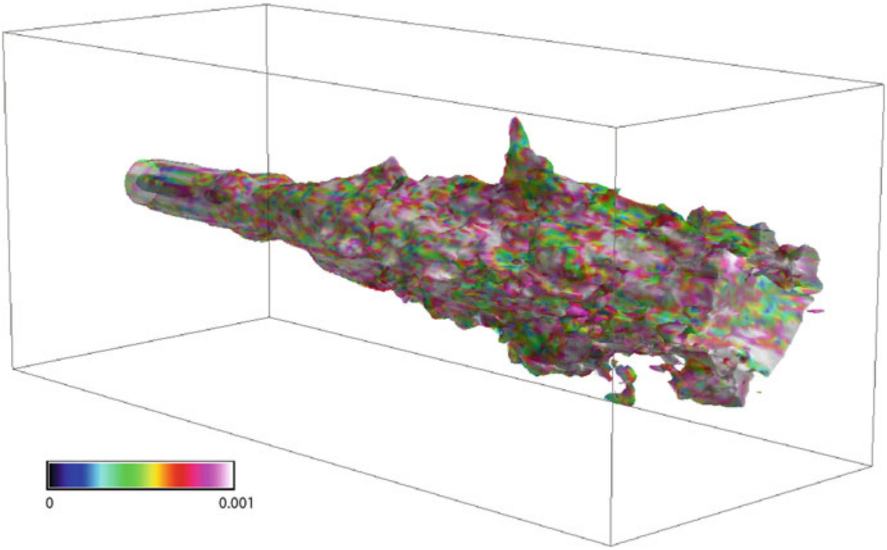

Fig. 3.4 Instantaneous vorticity magnitude iso-surface colored by SGS viscosity obtained via MKEV closure

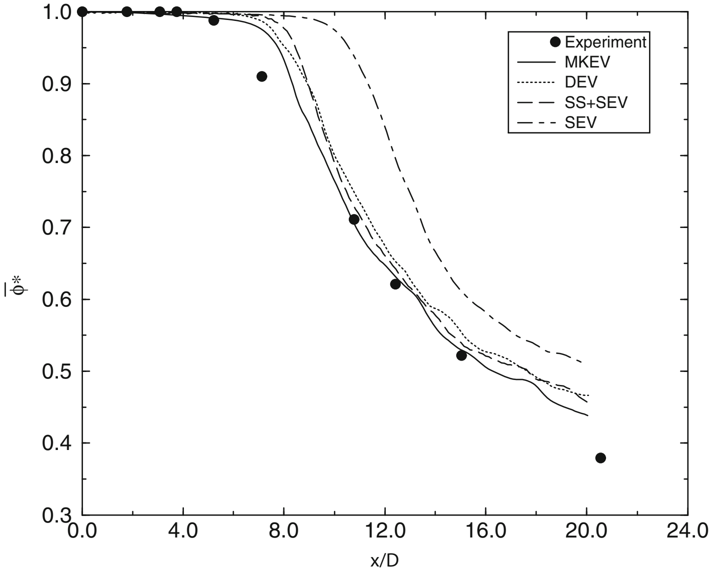

Fig. 3.5 Time-averaged, normalized propane mass fraction, $\overline{\phi^\star}$, along centerline ($r = 0$)

3.3.2 *Chemical Transport*

The performance of the SGS closures may be globally assessed by comparing the decay of species concentration along the centerline $r = 0$. The time-averaged propane mass fraction along the centerline is shown in Fig. 3.5. The figure reveals that all of the simulations exhibit a delay in the departure from unity, reflecting a delay in the breakdown of the jet. The MKEV model results in the earliest departure (nearest to the nozzle, $x/D = 0$) from $\phi^\star = 1$, occurring near $x/D = 7.5$, while the SEV model results in a departure occurring near $x/D = 10$. However, once the jets begin to transition from laminar to turbulent, the rate of decay is very similar to that observed in the experiment. This is reflected in the slope and shape of the curves in Fig. 3.5. The rate of decay can be quantified by considering the length of the jet potential core. The potential core length is defined as the point at which conserved scalar or species concentration is 85% of the jet-exit value, i.e., $\phi^\star = 0.85$. The potential core length obtained in the experiment is $9D$. The SEV closure yields a core length of $12.6D$, further indicating a reduced growth rate and delayed transition to turbulence observed in Fig. 3.3. The MKEV closure yields a core length of $9.1D$, the DEV closure yields a core length of $9.8D$, and the combined SS+SEV closure yields a core length of $9.8D$. The figure also reveals that the slope of the centerline concentration begins to change near $x/D = 16$ in all simulations. This may be due to the zero-derivative boundary conditions imposed at $x/D = 20$.

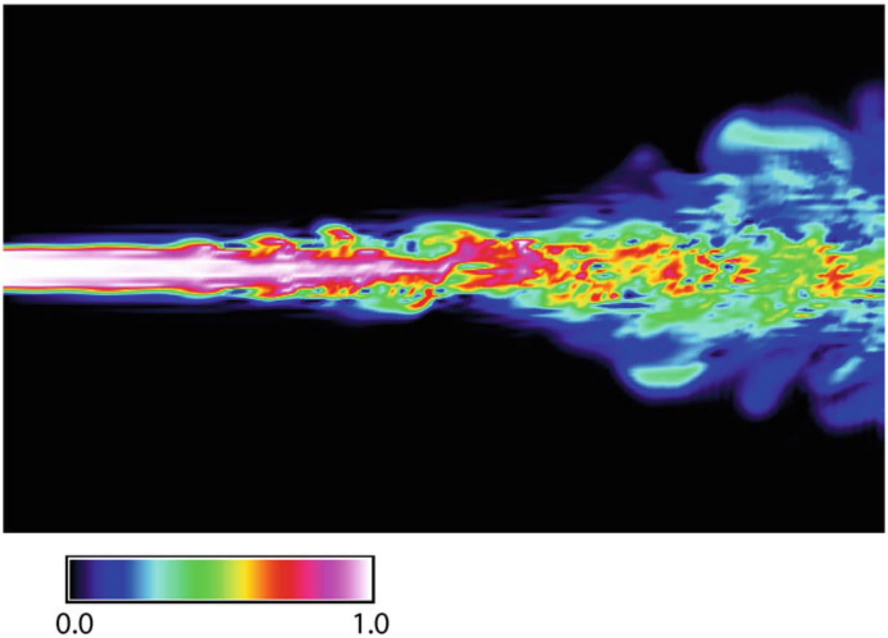

Fig. 3.6 Instantaneous propane mass fraction, $\phi^{\star}$, contours at $y = 0$ (MKEV)

The scalar field predicted by the LES is portrayed in Fig. 3.6. The image shows instantaneous contours of the normalized propane mass fraction $\phi^{\star} = \phi/(\phi)_{x=0,r=0}$ on the plane $y = 0$ obtained using the MKEV closure. The radial distribution of the propane mass fraction is shown in Fig. 3.7. The figure contains the time-averaged scalar at location $x/D = 15$. It is evident that the LES overpredicts the species mass fraction at all radial locations. For all simulations, except for the SEV model, the overprediction increases with radial distance from the centerline. The SEV model overpredicts the exact value by roughly 20% throughout the jet width.

3.3.3 *Performance Assessment*

The results lead us to use the MKEV closure in simulating the fluid–particle flows with mass transfer. The scale-similarity model was unable to yield a solution. All attempts at optimizing the value of the model constant C_S resulted in numerical instability. This may be due to a lack of dissipation. A solution was obtained by combining the Smagorinsky and the scale-similarity closures. The streamwise u-velocity obtained by the LES was compared to that measured in the experiment and found to be within 10%. All closures, except for the Smagorinsky, yielded values which were slightly more than the experimentally observed velocity. The

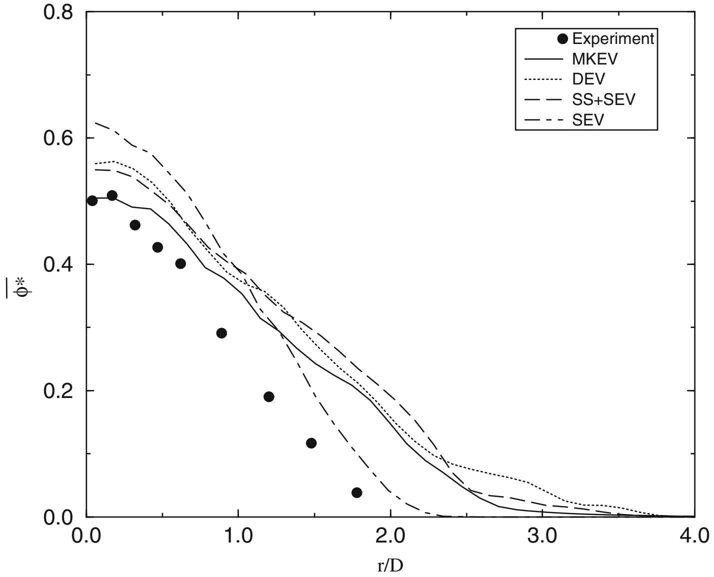

Fig. 3.7 Time-averaged radial propane mass fraction $\overline{\phi^\star}$ at $x/D = 15$

overprediction was greatest at the jet center and decreased with increasing radial position, eventually turning to an underprediction. This trend suggests that the Smagorinsky closure results in a reduced growth rate. This is further illustrated by the extended potential core predicted by the Smagorinsky closure which is 34% longer than that observed in the experiment. The other SGS closures are within 10% of the observed value. However, the results suggest that once the jet starts the transition from laminar to turbulent, all simulations predict the same rate of decay. This further underscores the fact that the prediction of the subgrid-scale quantities is not necessarily the deciding "characteristic" to be used in selection of a "good" subgrid-scale closure. Additionally, the computational requirements for the different closures are relatively the same. If the compute time is normalized by that of the Smagorinsky closure, then the modified kinetic energy viscosity closure requires 25% more time; the dynamic eddy viscosity closure requires 87% more time; and the combined scale-similarity/Smagorinksy closure requires 126% more time. In conclusion, while the dynamic eddy viscosity closure is appealing in that it does not require specification of any constants, it does not perform significantly better than the modified kinetic energy viscosity closure in the three-dimensional round jet considered.

3.4 LES of Gas-to-Particle Mass Transfer

We simulate a number of temporal mixing layers. Initially, the upper stream contains condensable vapor, and the lower stream contains uniformly distributed particles. As the flow evolves in time, vapor and particles are mixed, and mass is transferred from the gas phase to the particle phase through condensation. Three sets of parameters are considered. These are chosen from investigations in which carbon particles have been used as sorbent material to remove mercury vapor from gas as well as to establish consistency between the LES and DNS. To this end we adopt parameters that represent typical operating conditions of an ESP, typically employing Darco® G60 carbon blacks with a mean diameter $d_p = 20\,\mu\text{m}$, in accordance with [17]. The carrier gas is oxygen (N_2) at a temperature of $T = 425\,\text{K}$ containing trace amounts of mercuric chloride ($HgCl_2$). Sorption parameters for the carbon are extrapolated from data given by Karatza et al. [46]. The molecular diffusivity of elemental mercury (Hg) in nitrogen (N_2) is calculated with an expression for dilute gases given by Slattery and Bird [104]. Two particle Stokes numbers are used—$St_p = 0.1$ and $St_p = 10$—to establish the performance of the LES as the particle inertia (relative to the fluid) varies. Two mass Biot numbers are used—$Bi_m = 0$ and $Bi_m = 181.12$—as well as two Thiele numbers—$\Phi = 10$ and $\Phi = \infty$—to represent different intra-particle mass transfer. These parameters are tabulated in Table 3.1.

3.4.1 Assumptions

It is assumed that particles are spherical in shape with a homogeneous, porous structure. The particle diameter is much larger than the gas mean free path. Mass transport through solid (micropore diffusion) is neglected, that is, macropore diffusion is the dominant mass transfer process and obeys Fick's law [66, 88]. No phase change is involved in the isothermal mass transport process; only gaseous diffusion inside the pore network is considered [97]. We also assume that both the mass loading and volume loading of particles in the N_2 stream are sufficiently low so as to prevent kinetic energy exchange between the fluid and the particle, alteration of the fluid properties, and particle agglomeration.

Table 3.1 Particle transport and mass transfer properties

	Case A	Case B	Case C
Stokes number, St_p	10	0.1	0.1
Mass Biot number, Bi_m	0	0	181.12
Thiele number, Φ	∞	∞	10
Surface concentration, $C_s^\star$	0	0	0.95

3.4.2 Numerical Specifications

The governing fluid transport equations are solved using a MacCormack finite difference scheme [14, 67]. The accuracy of the scheme is second order in time and fourth order in space. A first-order accurate forward difference scheme is used to solve for the particle position, velocity, and mass as a function of time. The number of particles in the domain is $N_p = 50{,}000$. Since the fluid–particle transport equations are solved in a mixed Eulerian/Lagrangian framework, respectively, an interpolation algorithm is required to obtain the fluid transport variables at the particle locations. To this end, a linear interpolation scheme is used. Computations are performed on a domain of $2\pi \times 2\pi \times 1.2\pi$ in x, y, and z directions, respectively. Periodic boundary conditions are used in x and z directions, while free-stream boundary conditions are applied in y-direction. The periodic conditions imply that fluid and particles, exiting through the left, right, rear, or front boundaries, are reintroduced through the opposite boundary. The computational grid for the DNS is comprised of 768 × 768 × 480 evenly spaced grid points. The grid resolution is chosen such that the fluid field is grid independent. The LES grid is comprised of 32 × 32 × 24 grid points.

3.4.3 Fluid and Species Transport

The initial flow field is chosen such that two vortices are formed in streamwise direction. The images shown in Fig. 3.8 show the initial location of the particles and their subsequent transport across the mixing layer. Our first goal is to establish the accuracy or the performance of the LES. Using LES results in greatly reduced compute times—a 96% reduction—but that such savings are for nought if accuracy is lost. Both particle dispersion and mass transfer depend significantly on the

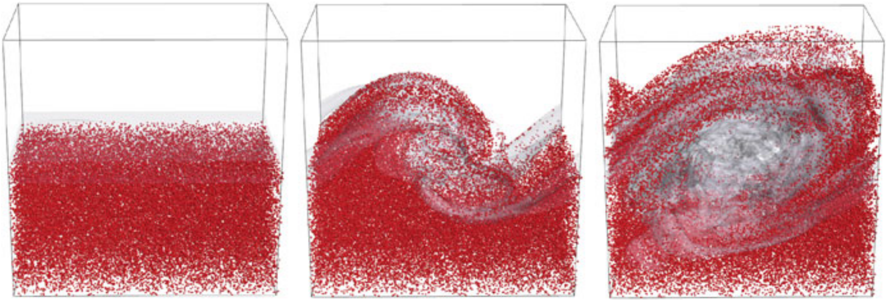

Fig. 3.8 Particle-laden temporal mixing layer flow configuration. Porous activated carbon particles are initially located in the lower half of the domain, while condensable mercury vapor (and carrier gas) is located in the upper half. The evolution of the mixing layer as predicted by LES (MKEV)

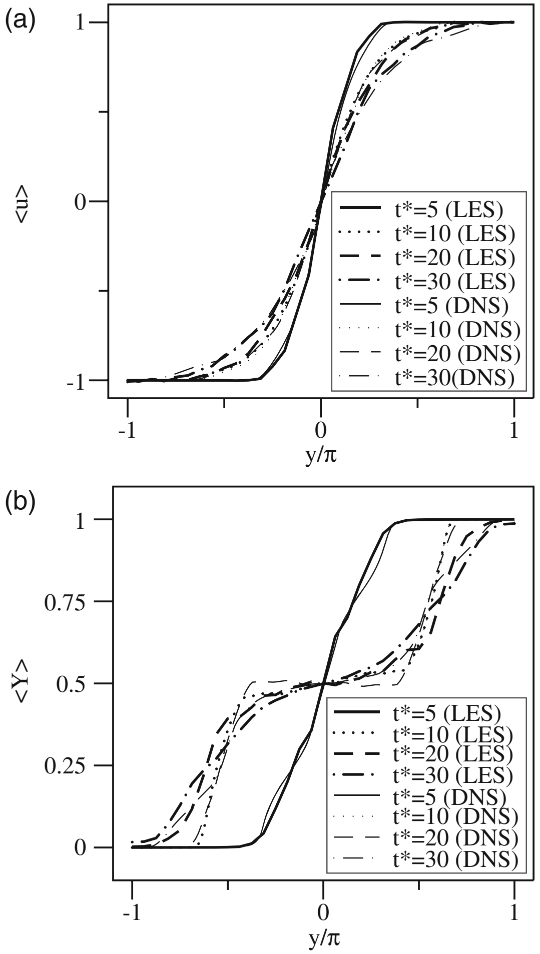

Fig. 3.9 Temporal evolution of (**a**) the stream-wise u-velocity and (**b**) mercury mass fraction (no adsorption), Y, across the mixing layer

velocity field. Cross-stream profiles of the velocity profile across the mixing layer are shown in Fig. 3.9a. The profiles show that the velocity gradient decreases across the shear layer as the two streams mix. This behavior is typical of temporal mixing layers, and nothing “new” is reported [38]. The LES results match the DNS results quite well. This suggests that our use of the SGS models in the momentum equations is justified and that, on average, the fluid velocity seen by the particles in the LES is quite similar to that of the DNS. We also performed simulations with no mercury adsorption. In these simulations mercury vapor—initially in the upper half of the domain ($y/\pi > 0$)—acts like a conserved scalar or a passive tracer. Cross-stream profiles of the normalized mercury mass fraction at four different times are shown in Fig. 3.9b. Again, the LES does a very good job in reproducing the mean mercury field of the DNS.

3.4.4 Particle Transport

With the fluid and species fields predicted by the LES in good agreement with those of the DNS, we turn our attention to the dynamics of the particles. The particles are initially located in the mercury-free portion of the domain/flow field. This mimics the entrainment during ACI [17]. Mercury capture is enhanced as the particles mix with the mercury-containing background gas, and, to this end, it is important that the particles are well dispersed. We quantify the dispersion of the particle field by computing the probability that particles are found at each location along the height of the mixing layer. As the particles move from the bottom ($y/\pi < 0$) to the top ($y/\pi > 0$), they move from the mercury-free to the mercury-laden gas. The probability density functions (PDFs), $f(y_p)$, denoting the probability of finding particles at location y/π for case A are shown in Fig. 3.10. The PDFs are shown at four different times, reflecting the formation and growth of the eddies that act to disperse the particles. In case A, the particle Stokes numbers is $St_p = 10$. At time

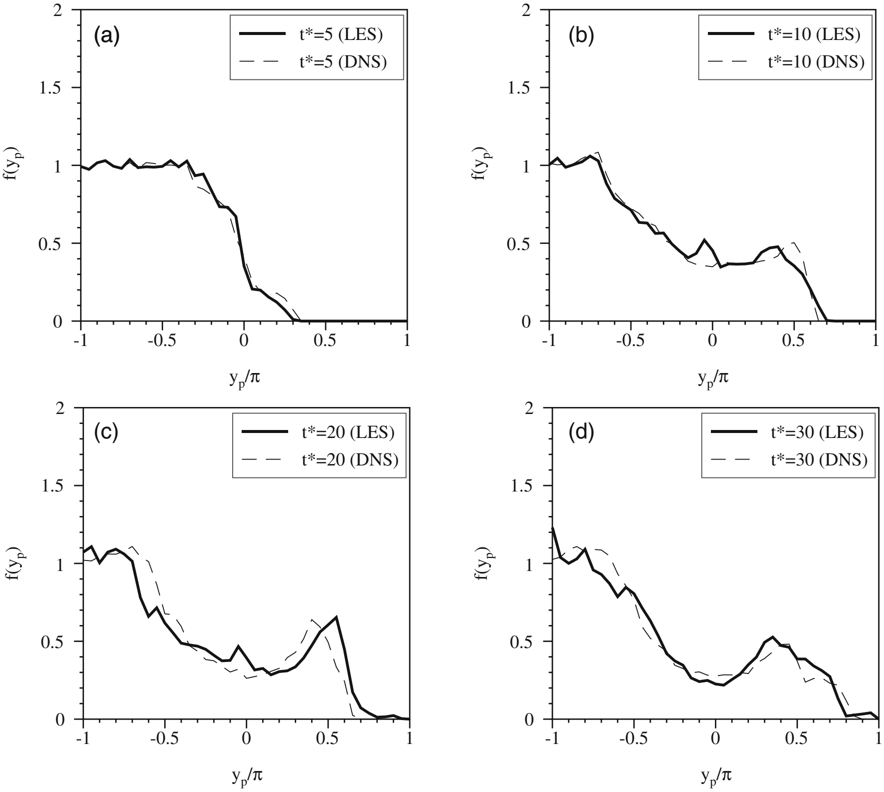

Fig. 3.10 Particle y-location probability density functions for case A at time: (**a**) $t^\star = 5$; (**b**) $t^\star = 10$; (**c**) $t^\star = 20$; (**d**) $t^\star = 30$

$t^\star = 0$ the function $f(y_p)$ is a step located at y/π, i.e., $f(y_p < 0) = 1$ and $f(y_p > 0) = 0$. Figure 3.10a shows that by time $t^\star = 5$, little migration across the mixing layer has occurred. In the DNS, a few more particles are found farther across the mixing layer as compared to the LES, but the results largely agree. At time $t^\star = 10$ the situation is similar to time $t^\star = 5$—good agreement between the LES and DNS except for a relatively large number of particles near $y/\pi = 0.5$ in the DNS. Figure 3.10b shows that the LES shows a similar number of particles near $y/\pi = 0$, suggesting that the LES lags the DNS. However, this trend is reversed at later times. At $t^\star = 20$ and $t^\star = 30$, shown in Fig. 3.10c and d, respectively, the LES predicts a greater number of particles dispersed into the mercury-laden stream ($y/\pi > 0$).

3.4.5 *Mercury Adsorption*

The ultimate goal is to establish the accuracy of the LES in predicting mercury adsorption. To do this we utilize instantaneous data, temporal data, and volume-integrated data. Such a view shows the details of the particle transport and mercury adsorption processes as well as the total amount of mercury removed from the gas. The first result is an instantaneous view of the mercury vapor, particle locations, and cumulative mercury captured, as well as the flow field, shown in Fig. 3.11.

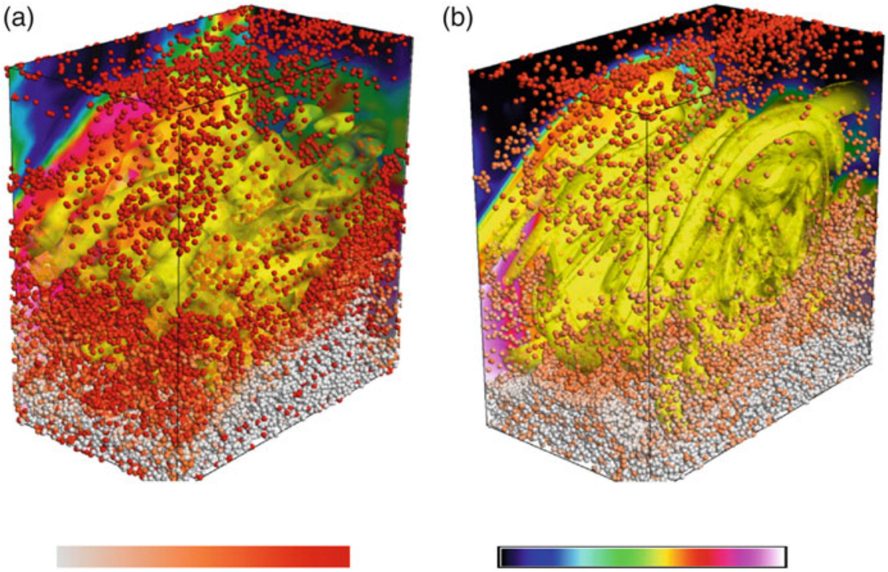

Fig. 3.11 Distribution of particles, condensed mass (a), condensable vapor (b), and vorticity contours (*yellow*) for case A at time $t^\star = 30$. LES result is on the *left* (**a**), and DNS is on the *right* (**b**)

Fig. 3.12 Temporal evolution of the total mercury vapor removed, Θ, from gas stream

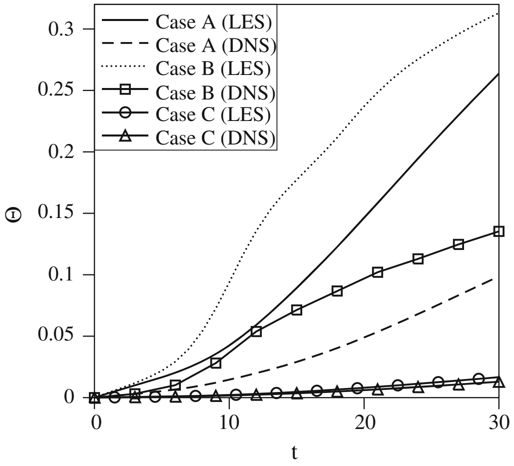

The image is taken at time $t^\star = 30$, the LES results are in Fig. 3.11a, and the DNS are in Fig. 3.11b. The differences in "resolution" are clearly observed in the vorticity iso-surface, shown in yellow. The DNS iso-surface contains more detail and fine-scale structure. It is such detail that leads to velocity fluctuations between the particle and the gas. While LES is not always characterized by a lack of velocity fluctuations, they are a significant factor in particle dispersion [70]. The overprediction of particle migration into the mercury-laden stream—quantified in Fig. 3.10d—is also evident. More particles are present in the top half of the domain in the LES (Fig. 3.11a) as compared to the DNS (Fig. 3.11b). The particle color reflects the mercury content—gray particles are entirely free of mercury, while the red particles have absorbed mercury from the gas. While both simulations show a large number of particles that have not come into contact with the mercury vapor, the results show that the mercury absorbed in the LES is significantly more than in the DNS.

The mercury absorbed by the porous particles in all three cases is shown in Fig. 3.12. The quantity Θ is defined as the amount of mercury transferred to the particle as a percentage of the total mercury in the flow. The particles in case A have a Stokes number of $St_p = 10$, while the particles in case B have a Stokes number of $St_p = 0.1$. That is the only difference between the simulations. The DNS results show that for case A, roughly 9% ($\Theta = 0.09$) of the mercury is removed from gas, while roughly 14% ($\Theta = 0.14$) of the mercury is removed in case B. This is due to faster particle dispersion into the mercury-laden stream. Once there they remain in contact with the mercury. This is evident as the amount of mercury removed in both flows is quite similar until time $t^\star = 7$. As shown in Fig. 3.10, the presence of particles in the mercury-laden gas increases significantly between $t^\star = 5$ and $t^\star = 10$. The particles in case B can be thought of as having less inertia which means that they are "swept up" by the fluid more quickly. The particles in case C have the same Stokes number as those in case B, but the porous structure of the particles is such that the concentration of mercury at the particle surface is roughly 95% of the gas concentration. For true carbon blacks, this concentration is between 95 and 99.9%. That is, the rate of mass transfer from the particle surface to its interior is rather slow. In case B (and case A), the concentration at the particle surface is identically zero. This is the perfect sink assumption and is a widely used simplification [69]. Figure 3.10 shows that the mercury removed in case B is roughly 1.5% ($\Theta = 0.015$).

3.5 Summary and Conclusions

In this chapter we performed LES of jets and mixing layers to characterize how the issues associated with modeling gas-to-particle mass transfer in shear flow. We assessed the performance of four LES approaches such as in predicting the fluid and scalar fields. In so doing we were able to choose the best SGS models for use in modeling particle transport. The dynamic SGS model and MKEV model yielded similar results. The MKEV model was used because it requires less CPU time. (The dynamic model requires multiple filtering operations which can be compute-intensive.)

The compute time associated with the LES is three orders of magnitude less than the DNS. This in itself is a significant savings. However there are dynamics that the LES is not able to capture. The lower-resolution simulations simply cannot reproduce the high-resolution velocity and concentration fields. As a result, the LES cannot fully replicate the alignment of particles and vortical structures. Additionally, the gas-to-particle mass transfer is not fully captured via LES. While the trends between the LES and the DNS are similar, the LES consistently overpredicts the amount of mercury captured by the particles. The difference between the LES and the DNS is the least in case C, where the LES overpredicts the mercury captured by roughly 30%. In both cases A and B, the LES overpredicts the DNS by roughly 130%.

This work suggests that the use of LES as a design tool or predictor of gas-to-particle mass transfer in turbulent flows must be used with proper caution. Even when the velocity and species fields are fairly well predicted, the nonlinear interactions between the particle, fluid, and species fields lead to significant differences. There is a need for models that are capable of representing the increased advection and diffusion to the particle surface present in turbulent flows.

References

1. Abram, J.C., Bennett, M.C.: Carbon blacks as model porous adsorbents. J. Colloid Interface Sci. **27**(1), 1–6 (1968)
2. Aldama, A.A.: Filtering techniques for turbulent flow simulations. Springer, New York (1990)
3. Apte, S.V., Mahesh, K., Moin, P., Oefelein, J.C.: Large-eddy simulation of swirling particle-laden flows in a coaxial-jet combustor. Int. J. Multiphase Flow **29**, 1311–1331 (2003)
4. Arpaci, V.S.: Conduction Heat Transfer. Pearson Custom Publishing, New York (1991)
5. Ausman, J.M., Watson, C.C.: Mass transfer in a catalyst pellet during regeneration. Chem. Eng. Sci. **17**, 323–329 (1962)
6. Bardina, J., Ferziger, J.H., Reynolds, W.C.: Improved subgrid scale models for large eddy simulation. AIAA Paper 80-1357 (1980)
7. Bardina, J., Ferziger, J.H., Reynolds, W.C.: Improved turbulence models based on large eddy simulations of homogeneous, incompressible, turbulent flows. Department of Mechanical Engineering Report TF-19, Stanford University, Stanford, CA (1983)
8. Barlow, R.S., Dibble, R.W., Chen, J.Y., Lucht, R.P.: Effects of Damkholer number on superequilibrium OH concentration in turbulent nonpremixed jet flames. Combust. Flame **82**, 235–251 (1990)
9. Bernal, L.P., Roshko, A.: Streamwise vortex structure in plane mixing layers. J. Fluid Mech. **170**, 499–525 (1986)
10. Boivin, M., Simonin, O., Squires, K.D.: Direct numerical simulation of turbulence modulation by particles in isotropic turbulence. J. Fluid Mech. **375**, 235–263 (1998)
11. Boivin, M., Simonin, O., Squires, K.D.: On the prediction of gas–solid flows with two-way coupling using large eddy simulation. Phys. Fluids **12**(8), 2080–2090 (2000)
12. Brown, G.L., Roshko, A.: On density effects and large structure in turbulent mixing layers. J. Fluid Mech. **64**, 775–816 (1974)
13. Calvert, S., Englund, H.M.: Handbook of Air Pollution Technology. Wiley, New York (1984)
14. Carpenter, M.H.: A high-order compact numerical algorithm for supersonic flows. In: Morton, K.W. (ed.) 12th International Conference on Numerical Methods in Fluid Dynamics. Lecture Notes in Physics, vol. 371, pp. 254–258. Springer, New York (1990)
15. Chorin, A.J.: Vorticity and Turbulence. Springer, New York (1994)
16. Clack, H.L.: Mass transfer within electrostatic precipitators: trace gas adsorption by sorbent-covered plate electrodes. J. Air Waste Manage. Assoc. **56**, 759–766 (2006)
17. Clack, H.L.: Mass transfer within electrostatic precipitators: in-flight adsorption of mercury by charged suspended particulates. Environ. Sci. Technol. **40**, 3617–3622 (2006)

S.C. Garrick, M. Bühlmann, *Modeling of Gas-to-Particle Mass Transfer in Turbulent Flows*, SpringerBriefs in Applied Sciences and Technology,
DOI 10.1007/978-3-319-59584-9

18. Clack, H.L.: Particle size distribution effects on gas–particle mass transfer within electostatic precipitators. Environ. Sci. Technol. **40**, 3929–3933 (2006)
19. Colucci, P.J., Jaberi, F.A., Givi, P., Pope, S.B.: Filtered density function for large eddy simulation of turbulent reacting flows. Phys. Fluids **10**(2), 499–515 (1998)
20. Crow, S.C., Champagne, F.H.: Orderly structure in jet turbulence. J. Fluid Mech. **48**, 547–591 (1971)
21. Cunningham, R.E., Williams, R.J.J.: Diffusion in Gases and Porous Media. Plenum Press, New York (1980)
22. Damköhler, G.: über die adsorptionsgeschwindigkeit von gasen an porösen adsorbentien. Z. Phys. Chem. **174**, 222–238 (1935)
23. Danaila, I., Dusek, J., Anselmet, F.: Coherent structures in a round, spatially evolving, unforced, homogeneous jet at low Reynolds numbers. Phys. Fluids **9**(11), 3323–3342 (1997)
24. Davis, W.T.: Air Pollution Engineering Manual, 2nd edn. Wiley, New York (2000)
25. Drazin, P.G., Reid, W.H.: Hydrodynamic Stability. Cambridge University Press, New York (1981)
26. Eidson, T.M.: Numerical simulation of the turbulent Rayleigh-Benard problem using subgrid modelling. J. Fluid Mech. **158**, 245–268 (1985)
27. Ferziger, J.H.: Higher level simulations of turbulent flows. Stanford University Report TF-16, Department of Mechanical Engineering, Stanford University, Stanford, CA (1981)
28. Ferziger, J.H.: Large eddy simulations: its role in turbulence research. In: Dwoyer, D.L., Hussaini, M.Y., Voigt, R.G. (eds.) Theoretical Approaches in Turbulence, pp. 51–72. Springer, New York (1987)
29. Flora, J.R.V., Hargis, R.A., O'Dowd, W.J., Pennline, H.W., Vidic, R.D.: Modeling sorbent injection for mercury control in baghouse filters: I—model development and sensitivity analysis. J. Air Waste Manage. Assoc. **53**, 478–488 (2003)
30. Friedlander, S.K.: Smoke, Dust, and Haze: Fundamentals of Aerosol Dynamics, 2nd edn. Oxford University Press, New York (2000)
31. Friesen, W.I., Mikula, R.J.: Fractal dimensions of coal particles. J. Colloid Interface Sci. **120**(1), 263–271 (1987)
32. Frössling, N.: über die verdunstung fallender tropfen. Gerlands Beitr. Geophys. **52**, 170–215 (1938)
33. Galperin, B., Orszag, S.A. (eds.): Large Eddy Simulations of Complex Engineering and Geophysical Flows. Cambridge University Press, Cambridge (1993)
34. Garrick, S.C., Jaberi, F.A., Givi, P.: Large eddy simulation of scalar transport in a turbulent jet flow. In: Knight, D., Sakell, L. (eds.) Recent Advances in DNS and LES. Fluid Mechanics and Its Applications, vol. 54, pp. 155–166. Kluwer Academic Publishers, The Netherlands (1999)
35. Germano, M.: Turbulence: the filtering approach. J. Fluid Mech. **238**, 325–336 (1992)
36. Germano, M., Piomelli, U., Moin, P., Cabot, W.H.: A dynamic subgrid-scale eddy viscosity model. Phys. Fluids A **3**(7), 1760–1765 (1991)
37. Gicquel, L.Y.M., Givi, P., Jaberi, F.A., Pope, S.B.: Velocity filtered density function for large eddy simulation of turbulent flows. Phys. Fluids **14**(3), 1196–1214 (2002)
38. Givi, P.: Model free simulations of turbulent reactive flows. Prog. Energy Combust. Sci. **15**, 1–107 (1989)
39. Guan, G., Zhu, J., Xia, S., Feng, Z., Davis, E.J.: Simulation of mass transfer from an oscillating microdroplet. Int. J. Heat Mass Transf. **48**, 1705–1715 (2005)
40. Harrison, B.H.: Characterization of superactivated carbons. J. Colloid Interface Sci. **71**(2), 367–374 (1979)
41. Hinds, W.C.: Aerosol Technology: Properties, Behavior, and Measurement of Airborne Particles, 2nd edn. Wiley, New York (1999)
42. Hwang, W., Eaton, J.K.: Homogeneous and isotropic turbulence modulation by small heavy ($st \sim 50$) particles. J. Fluid Mech. **564**, 361–393 (2006)
43. Ishida, M., Wen, C.Y.: Comparison of kinetic and diffusional models for solid–gas reactions. AlChE J. **14**(2), 311–317 (1968)

44. Jaberi, F.A., Colucci, P.J., James, S., Givi, P., Pope, S.B.: Filtered mass density function for large eddy simulation of turbulent reacting flows. J. Fluid Mech. **401**, 85–121 (1999)
45. Karatza, D., Lancia, A., Musmarra, D., Pepe, F., Volpicelli, G.: Kinetics of adsorption of mercuric chloride vapors on sulfur impregnated activated carbon. Combust. Sci. Technol. **112**, 163–174 (1996)
46. Karatza, D., Lancia, A., Musmarra, D., Pepe, F., Volpicelli, G.: Removal of mercuric chloride from flue gas by sulfur impregnated activated carbon. Hazard. Waste Hazard. Mater. **13**(1), 95–105 (1996)
47. Karatza, D., Lancia, A., Musmarra, D.: Fly ash capture of mercuric chloride vapors from exhaust combustion gas. Environ. Sci. Technol. **32**, 3999–4004 (1998)
48. Kennedy, C.A., Carpenter, M.H.: Several new numerical methods for compressible shear-layer simulations. Appl. Numer. Math. **14**, 397–433 (1994)
49. Kiger, K.T., Lasheras, J.C.: Dissipation due to particle/turbulence interaction in a two-phase turbulent, shear layer. Phys. Fluids **9**(10), 3005–3023 (1997)
50. Knight, D., Sakell, L. (eds.): Recent Advances in DNS and LES. Fluid Mechanics and its Applications. Kluwer Academic Press, The Netherlands (1993)
51. Krishnan, S.V., Gullett, B.K., Jozewicz, W.: Sorption of elemental mercury by activated carbons. Environ. Sci. Technol. **28**, 1506–1512 (1994)
52. Kuan, B.T.: CFD simulation of dilute gas-solid two-phase flows with different solid size distributions in a curved 90 ° duct bend. ANZIAM J. **46**, C744–C763 (2005)
53. Lancia, A., Karatza, D., Musmarra, D., Pepe, F.: Adsorption of mercuric chloride from simulated incinerator exhaust gas by means of Sorbalit$^{\text{TM}}$ particles. J. Chem. Eng. Jpn. **29**(6), 939–946 (1996)
54. Langmuir, I.: The adsorption of gases on plane surfaces of glass, mica and platinum. J. Am. Chem. Soc. **40**, 1361–1403 (1918)
55. Le Clercq, P.C., Bellan, J.: Direct numerical simulation of a transitional temporal mixing layer laden with multicomponent-fuel evaporating drops using continuous thermodynamics. Phys. Fluids **16**(6), 1884–1907 (2004)
56. Lide, D.R. (ed.): Handbook of Chemistry and Physics CRCnet BASE 2000, 79th edn. RAmEX, Inc, Los Angeles (2000)
57. Liepmann, D.: Streamwise vorticity and entrainment in the near field entrainment of a round jet. Phys. Fluids A. **3**(5), 1179–1187 (1991)
58. Liepmann, D., Gharib, M.: The role of streamwise vorticity in the near field entrainment of round jets. J. Fluid Mech. **245**, 643–668 (1992)
59. Lilly, D.K.: On the computational stability of numerical solutions of time-dependent non-linear geophysical fluid dynamics problems. Mon. Weather Rev. **93**(1), 11–26 (1965)
60. Lilly, D.K.: A proposed modification of the Germano subgrid-scale closure method. Phys. Fluids A **4**(3), 633–634 (1992)
61. Ling, W., Chung, J.N., Troutt, T.R., Crowe, C.T.: Direct numerical simulation of a three-dimensional temporal mixing layer with particle dispersion. J. Fluid Mech. **358**, 61–85 (1998)
62. Liu, S., Meneveau, C., Katz, J.: On the properties of similarity subgrid-scale models as deduced from measurements in a turbulent jet. J. Fluid Mech. **275**, 83–119 (1994)
63. Liu, C., Sakell, L., Beutner, T. (eds.): DNS/LES – Progress and Challenges. Greyden Press, Columbus (2001)
64. Logan, B.E.: Environmental Transport Processes. Wiley, Hoboken (1999)
65. Love, M.D.: An introduction to the large eddy simulation technique. J. Inst. Nucl. Eng. **20**(2), 35–42 (1979)
66. Ma, Y.H., Lee, T.Y.: Transient diffusion in solids with a bipore distribution. AlChE J. **22**(1), 147–152 (1976)
67. MacCormack, R.W.: The effect of viscosity in hypervelocity impact cratering. AIAA Paper 69–354 (1969)
68. Madsen, J.I., Rogers, W.A., O'Brien, T.J.: Computational modeling of mercury control by sorbent injection. In: Proceedings of ASME Power 2004, 30 March–1 April, Baltimore, MD, USA (2004)

69. Madsen, J.I., Starns, T., Rogers, W.A., O'Brien, T.J.: The impact of turbulent mixing on sorbent dispersion in coal-derived flue gas. In: International Conference on Air Quality V, 19–21 September 2005, Arlington, VA, USA (2005)
70. Marchioli, C., Salvetti, M.V., Soldati, A.: Some issues concerning large-eddy simulation of inertial particle dispersion in turbulent bounded flows. Phys. Fluids **20**(4), 040603 (2008). doi:10.1063/1.2911018
71. Martin, M.P., Candler, G.V.: Subgrid-scale models for compressible LES. Theor. Comput. Fluid Dyn. **13**, 361–376 (2000)
72. Meserole, F.B., Chang, R., Carey, T.R., Machac, J., Richardson, C.F.: Modeling mercury removal by sorbent injection. J. Air Waste Manage. Assoc. **49**, 694–704 (1999)
73. Miller, R.S., Bellan, J.: Direct numerical simulation of a confined three-dimensional gas mixing layer with one evaporating hydrocarbon-droplet-laden stream. J. Fluid Mech. **384**, 293–338 (1999)
74. Miller, R.S., Bellan, J.: Direct numerical simulation and subgrid analysis of a transitional droplet laden mixing layer. Phys. Fluids **12**(3), 650–671 (2000)
75. Moser, R.D., Rogers, M.M.: The three-dimensional evolution of a plane mixing layer: pairing and transition to turbulence. J. Fluid Mech. **247**, 275–320 (1993)
76. Narayanan, C., Lakehal, D.: Particle transport and flow modification in planar temporally evolving laminar mixing layers. I. Particle transport under one-way coupling. Phys. Fluids **18**, 093302–1–15 (2006)
77. Narayanan, C., Lakehal, D.: Particle transport and flow modification in planar temporally evolving laminar mixing layers. II. Flow modification due to two-way coupling. Phys. Fluids **18**, 093,303–1–13 (2006)
78. Narayanan, C., Lakehal, D., Yadigaroglu, G.: Linear stability analysis of particle-laden mixing layers using lagrangian particle tracking. Powder Technol. **125**, 122–130 (2002)
79. Oppenheim, A.V., Schafer, R.W.: Discrete-Time Signal Processing. Prentice Hall, Englewood Cliffs (1989)
80. Pope, S.B.: Turbulent Flows. Cambridge University Press, Cambridge (2000)
81. Ranz, W.E., Marshall, W.R.: Evaporation from drops, part I. Chem. Eng. Prog. **48**(3), 141–146 (1952)
82. Ranz, W.E., Marshall, W.R.: Evaporation from drops, part II. Chem. Eng. Prog. **48**(4), 173–180 (1952)
83. Rawlings, J.B., Ekerdt, J.G.: Chemical Reactor Analysis and Design Fundamentals. Nob Hill Publishing, Madison (2002)
84. Rogallo, R.S., Moin, P.: Numerical simulation of turbulent flow. Ann. Rev. Fluid Mech. **16**, 99–137 (1984)
85. Roshko, A.: Structure of turbulent shear flows: a new look. AIAA J. **14**(10), 1349–1357 (1976)
86. Rosner, D.E.: Transport processes in chemically reacting flow systems. Butterworth, Boston (1986)
87. Ruckenstein, E., Vaidyanathan, A.S., Youngquist, G.R.: Sorption by solids with bidisperse pore structures. Chem. Eng. Sci. **26**, 1305–1318 (1971)
88. Ruthven, D.M.: Principles of Adsorption and Adsorption Processes. Wiley, New York (1984)
89. Rütten, F., Meinke, M., Schröder, W.: Large-eddy simulations of 90° pipe bend flows. J. Turbul. **2**, 1–14 (2001)
90. Sagaut, P.: Large-Eddy Simulations for Incompressible Flows: An Introduction. Scientific Computation, 2nd edn. Springer, Berlin (2001)
91. Sahin, E., Dogu, T., Mürtezaoğlu, K.: Thermal effects on effectiveness of catalysts having bidisperse pore size distribution. Chem. Eng. J. **93**, 143–149 (2003)
92. Salazar, J.P.L.C., de Jong, J., Cao, L., Woodward, S., Meng, H., Collins, L.R.: Experimental and numerical investigation of inertial particle clustering in isotropic turbulence. J. Fluid Mech. **600**, 245–256 (2008)
93. Salvetti, M.V., Banerjee, S.: A priori tests of a new dynamic subgrid-scale model for finite-difference large-eddy simulations. Phys. Fluids **7**(11), 2831–2847 (1995)

94. Sami, S., Carmody, T., Rouse, H.: Jet diffusion in the region of flow establishment. J. Fluid Mech. **27**, 231–252 (1967)
95. Samimy, M., Lele, S.K.: Motion of particles with inertia in a compressible free shear layer. Phys. Fluids **3**(8), 1915–1923 (1991)
96. Sandham, N.D., Reynolds, W.C.: Three-dimensional simulations of large eddies in the compressible mixing layer. J. Fluid Mech. **224**, 133–158 (1991)
97. Scala, F.: Simulation of mercury capture by activated carbon injection in incinerator flue gas. 1. In-duct removal. Environ. Sci. Technol. **35**, 4367–4372 (2001)
98. Scala, F.: Simulation of mercury capture by activated carbon injection in incinerator flue gas. 2. Fabric filter removal. Environ. Sci. Technol. **35**, 4373–4378 (2001)
99. Scala, F.: Modeling mercury capture in coal-fired power plant flue gas. Ind. Eng. Chem. Res. **43**, 2575–2589 (2004)
100. Schefer, R.W.: Data base for a turbulent, nonpremixed nonreacting propane-jet flow. Technical Report, Combustion Research Facility Sandia National Laboratories, Livermore, CA (1985)
101. Schumann, U., Friedrich, R. (eds.): Direct and Large Eddy Simulations of Turbulence: Proceedings of the EUROMECH Colloquium No. 199. Vieweg-Verlag, Braunschweig (1986)
102. Serre, S.D., Silcox, G.D.: Adsorption of elemental mercury on the residual carbon in coal fly ash. Ind. Eng. Chem. Res. **39**, 1723–1730 (2000)
103. Sherwood, T.K., Pigford, R.L., Wilke, C.R.: Mass Transfer. McGraw-Hill, New York (1975)
104. Slattery, J.C., Bird, R.B.: Calculation of the diffusion coefficient of dilute gases and of the self-diffusion coefficient of dense gases. AlChE J. **4**(2), 137–142 (1958)
105. Smagorinsky, J.: General circulation experiments with the primitive equations. I. The basic experiment. Mon. Weather Rev. **91**(3), 99–164 (1963)
106. Smith, L.L., Dibble, R.W., Talbot, L., Barlow, R.S., Carter, C.D.: Laser Raman scattering measurements of differential molecular diffusion in nonreacting turbulent jets of H_2/CO_2 mixing with air. Phys. Fluids **7**(6), 1455–1466 (1995)
107. Squires, K.D., Eaton, J.K.: Preferential concentration of particles by turbulence. Phys. Fluids A **3**(5), 1169–1178 (1991)
108. Strykowski, P.J., Niccum, D.L.: Jet diffusion in the region of flow establishment. J. Fluid Mech. **227**, 309–343 (1991)
109. Tannehil, J.C., Anderson, D.A., Pletcher, R.H.: Computational Fluid Mechanics and Heat Transfer, 2nd edn. Taylor and Francis, Washington (1997)
110. Thiele, E.W.: Relation between catalytic activity and size of particle. Ind. Eng. Chem. **31**(7), 916–920 (1939)
111. Tu, J.Y., Fletcher, C.A.J.: Numerical computation of turbulent gas-solid particle flow in a 90° bend. AlChE J. **41**, 2187–2197 (1995)
112. U.S. EPA: Mercury study report to congress volume I: executive summary (epa-452/r-97-003). Technical Report, U.S. Environmental Protection Agency (1997)
113. Voke, P.R., Collins, M.W.: Large eddy simulation: retrospect and prospects. PhysicoChem. Hydrodyn. **4**(2), 119–161 (1983)
114. Vreman, B., Geurts, B., Kuerten, H.: Large-eddy simulations of the turbulent mixing layer. J. Fluid Mech. **339**, 357–390 (1997)
115. Wang, Q., Squires, K.D.: Large eddy simulation of particle-laden turbulent channel flow. Phys. Fluids **8**(5), 1207–1223 (1996)
116. White, H.J.: Industrial Electrostatic Precipitation. Addison-Wesley, Reading, MA (1963)
117. Wygnanski, I., Fiedler, H.: Some measurements in the self-preserving jet. J. Fluid Mech. **38**, 577–612 (1969)
118. Yan, Y., Peng, X.F., Lee, D.J.: Transport and reaction characteristics in flue gas desulfurization. Int. J. Therm. Sci. **42**, 943–949 (2003)
119. Youngquist, G.R., Allen, J.L., Eisenberg, J.: Adsorption of hydrocarbons by synthetic zeolites. Ind. Eng. Chem. Prod. Res. Dev. **10**, 308–314 (1971)
120. Zhu, J., Zheng, F., Laucks, M.L., Davis, E.J.: Mass transfer from an oscillating microsphere. J. Colloid Interface Sci. **249**, 351–358 (2002)